Formation of rutile (Cr,Ta,Ti)O_2 oxides during oxidation of refractory high entropy alloys in Ta-Mo-Cr-Ti-Al system

Authors

S. Schellert [a], M. Weber [a], H. J. Christ [a], C. Wiktor [b], B. Butz [b], M. C. Galetz [c], S. Laube [d], A. Kauffmann [d], M. Heilmaier [d], and B. Gorr [e,*]

steven.schellert@uni-siegen.de; mathias.weber@uni-siegen.de; hans-juergen.christ@uni-siegen.de; christian.wiktor@uni-siegen.de; benjamin.butz@uni-siegen.de; galetz@dechema.de; stephan.laube@kit.edu; alexander.kauffmann@kit.edu; martin.heilmaier@kit.edu; bronislava.gorr@kit.edu

Affiliation

[a]Institut für Werkstofftechnik, Universität Siegen, Paul-Bonatz-Str. 9-11, 57068 Siegen, Germany;

[b]Lehrstuhl für Mikro- und Nanoanalytik und -tomographie, Universität Siegen, Paul-Bonatz-Str. 9-11, 57068 Siegen, Germany;

[c]DECHEMA-Forschungsinstitut, Hochtemperaturwerkstoffe, Theodor-Heuss-Allee 25, 60486 Frankfurt am Main, Germany

[d]Institut für Angewandte Materialien–Werkstoffkunde (IAM-WK), Karlsruhe Institut für Technologie (KIT), Engelbert-Arnold-Str. 4, 76131 Karlsruhe, Germany;

[e]Institut für Angewandte Materialien– Angewandte Werkstoffphysik (IAM-AWP), Karlsruhe Institut für Technologie (KIT), Hermann-von Helmholzt-Platz 1, 76344 Eggenstein-Leopoldshafen, Germany;

[*] corresponding author:
mail: bronislava.gorr@kit.edu

Abstract:
The chemical identity of rutile oxides formed during oxidation of alloys with different Ti content within the Ta-Mo-Cr-Ti-Al system at 1200°C for 24h was determined. Rutile-type oxide (Cr,Ta,Ti)O_2 was observed on 20Ta20Mo20Cr20Ti20Al and 67.5(TaMoCr)10Ti22.5Al (at.%). Based on the experimental results, the valence states of Cr, Ta and Ti were unequivocally determined. Higher concentrations of Ti in (Cr,Ta,Ti)O_2 lead to the formation of thinner oxide scales and zones of internal corrosion. It is conluded that the occupation of higher-valent Ti^{4+} cations on the Cr^{3+} sub-lattice reduces the oxygen vacancy concentration and thus improves the oxidation behaviour of n-type conducting (Cr,Ta,Ti)O_2-forming alloys.

Keywords: refractory high entropy alloy, rutile (Cr,Ta)O_2, rutile (Cr,Ta,Ti)O_2, oxidation state analysis, TEM-EELS

Highlights

Cation oxidation states of (Cr,Ta,Ti)O_2, formed on alloys in the Ta-Mo-Cr-Ti-Al system were determined by electron energy-loss spectroscopy.

The protective properties of rutile (Cr,Ta,Ti)O_2 are discussed based on the Wagner-Hauffe valence approach.

A map of the lattice parameters of various transition metal-based rutile oxides is provided.

1. Introduction

Despite their attractive high-temperature strength [1–10], a significant drawback of most Refractory High Entropy Alloys (RHEAs) represents their poor oxidation behaviour [11–19], attributed to the insufficient oxidation resistance of pure refractory metals (RMs). Pure and low alloyed RM form porous and fast-growing oxides, like WO_3 [20,21], Nb_2O_5 [22,23] and Ta_2O_5 [24], or volatile oxides, like V_2O_5 [16,25], MoO_3 [21,25] and WO_3 [25,26] depending on temperature and oxygen partial pressure. In addition, most RMs as well as the group IV elements such as Zr [27], α-Hf [28] and α-Ti [29,30], which are often constituents of RHEAs, possess very high oxygen solubility. But this property does not apply to RMs such as W [31,32] and Mo [32], which feature a very low oxygen solubility in contrast. To improve the high-temperature oxidation resistance of RHEAs according to the classical concept, the elements Cr, Al or Si are added to form protective scales of Cr_2O_3, Al_2O_3 or SiO_2, respectively [33–41]. The majority of common RHEAs form thick, non-protective oxide layers consisting of mixed oxides [14,17–19,42–48]. Zr- and V-containing RHEAs display the lowest high-temperature oxidation resistance and a high mass gain after oxidation at 1000 °C for 10 h [16–19]. The high oxygen solubility in the metallic bulk of TiZrNbHfTa [48] and Hf0.5Nb0.5Ta0.5Ti1.5Zr [44] in combination with the formation of non-protective ZrO_2 lead to a pronounced internal diffusion zone with cracking due to growth stresses and subsequent spallation. In V-containing alloys such as CrMoNbTaV the formation of liquid or gaseous V_2O_5 along with MoO_3 evaporation prevents the formation of a protective oxide layer [19]. Even the passivating elements Cr and Al are unable to significantly improve the oxidation behaviour [17,42,48]. In the case of Nb-containing and W-containing RHEAs, like NbMoCrTiAl [45] and NbCrVWTa [49], voluminous Nb_2O_5 (Pilling Bedworth ratio; PBR = 2.5) and WO_3 (PBR = 3.3) are observed, which lead to rupture of the oxide layer and accelerate oxygen inward diffusion. The reason for the non-protective properties of the Nb-containing oxides is probably related to multiple polymorphic modifications of Nb_2O_5 [50,51]. Especially the β-Nb_2O_5 modification is known for the highest volume expansion and causing crack formation and chipping [45,52,53]. The multifarious formation of complex oxides such as Cr_2TiO_5 [18], $TiNb_2O_7$ [17], $(Ti_{1.5}Ta_{0.5}Nb_{0.5}Hf_{0.5}Zr)O_8$ [44], $Nb_2Zr_6O_{17}$ [17], $(Ti,Cr,Nb)O_2$ [54] or $CrVNbO_6$ [54] is reported. However, those as well do not offer protection against severe oxidation. Only a very few RHEAs are capable of forming protective oxide scales [45,55,56]. The formation of a protective Al_2O_3 layer was exclusively reported for $Nb_{1.3}Si_{2.4}Ti_{2.4}Al_{3.5}Hf_{0.4}$ after oxidation at 1200 °C for 100 h [56]. Moreover, some Cr-, Al-, Ta- and Ti-containing RHEAs demonstrate considerable oxidation resistance [45–47,55,57]. In those cases, the beneficial effect on the oxidation behaviour is attributted to the chemical reaction of simple oxides to the more complex ones [45–47,55,57]. The 13.4Ta15.2Nb20.3Mo25.2Cr5.4Ti17.6Al2.9Si (at.%) is protected against catastrophic oxidation by the formation of a rutile $CrTaO_4$ based oxide layer during oxidation at both 1000 °C and 1100 °C for 200 h [55]. Our preliminary studies on TaMoCrTiAl indicate that a protective rutile Cr-Ta oxide layer acts as a barrier to cation outward diffusion and in conjunction reduces oxygen inward diffusion in the temperature range of 500 °C – 1500°C [45,47,58]. However, the protective properties of complex oxide grown on RHEAs have not been understood in detail. The previous studies reveal that a complex rutile Cr-Ta oxide is formed during the oxidation of TaMoCrTiAl at 1200 °C for 24 h, whereby a considerable amount of Ti is dissolved in such [45,47]. Transition metals like Ti within those oxides are known to adapt to different oxidation states, e.g. Ti^{2+} in TiO, Ti^{3+} in Ti_2O_3, or Ti^{4+} in TiO_2 [59]. The stoichiometry, the oxidation states as well as the defect structure of the rutile Cr-Ta-Ti oxide formed on the equiatomic alloy Ta-Mo-Cr-Ti-Al are not clear yet.

In this work, chemical stoichiometry and the oxidation states with in the respective rutile Cr-Ti-Ta oxides grown on RHEAs with varying Ti contents, i.e. 20Ta20Mo20Cr20Ti20Al, 67.5(TaMoCr)10Ti22.5Al, 25Ta25Mo25Cr25Al (at.%) are determined and correlated to their oxidation resistance. Particulary, the impact of Ti on the protective properties of oxide scales was clarified. To generally understand the nature of the oxides formed in mentioned alloys within the Ta-Mo-Cr-Ti-Al system, additional alloys 20Ta80Cr (at.%) and equimolar TaCrTi were manufactured, oxidized and their scales investigated by X-ray diffraction (XRD) and transmission electron microscopy (TEM). The microstructure of both additional alloys as well as the oxidation kinetics were not thoroughly studied. The additional alloy 20Ta80Cr was selected because is kown to form a Cr-Ta oxide on the Laves phase underneath a covering Cr_2O_3 top layer during oxidation at 1100 °C for 24 h [60]. The alloy TaCrTi is related to the elements Ta, Cr, Ti, which are the constituents of rutile Ta-Cr-Ti oxide. To achieve the objective stated above, a cross-scale materials analysis is applied, including STEM-EELS electron energy-loss spectroscopy (EELS) in combination with scanning transmission electron microscopy (STEM) [61–63]. The oxidation products of two additional alloys (20Ta80Cr and TaCrTi) in combination with Cr_2O_3, Ta_2O_5, and TiO_2 powders provide EELS references to unambiguously identify the oxidation states of formed rutile Cr-Ta-(Ti) oxides on high entropy alloys in Ta-Mo-Cr-Ti-Al system. The

oxidation states as well as quantitative energy dispersive X-Ray spectroscopy in STEM (STEM-EDX) serve as a basis for the discussion of the protective properties of the different formed oxides.

2. Experimental Procedures

All investigated alloys were manufactured from elemental bulk material by arc melting (AM/0,5 Arc melting furnace by company Edmund Bühler GmbH). The pure elements Ta, Mo, Cr, Ti and Al were supplied by chemPUR GmbH. Purities of the elements Ta, Mo, Cr, Ti and Al are 99.9, 99.95, 99.99, 99.8 and 99.99 %, respectively. The elements were carefully weighed according to the desired chemical composition of the alloys and (re-)melted at least five times under ≈ 0.6 atm of Ar in the water-cooled mold of the arc melter. To dissolve the dendritic microstructure, all alloys were homogenized at 1500 °C for 20 h in flowing Ar protective gas (HTRT 70-600/18 tube furnace by Carbolite Gero GmbH & Co. KG). Subsequently, the alloys were cooled down to room temperature in the furnace. The applied heating and cooling rates were 250 K/h. The chemical compositions of the alloys were confirmed by inductively coupled plasma optical emission spectrometry (ICP-OES) (TaMoCrTiAl [47]**)** as well as energy dispersive X-ray spectroscopy in the scanning electron microscope (SEM-EDX; k-factors provided in the employed software TEAM™ V4.5.1 see Table 1). The ICP-OES results of TaMoCrTiAl served as a reference for the SEM-EDX measurements of the alloy samples. All alloy compositions are in very well agreement with the desired compositions within the maximum deviation of 0.5 %.

Table 1: Chemical composition $\bar{x}$ [at. %] of investigated alloys in annealed condition (1500 °C, 20 h) as derived from SEM-EDX. (Only the chemical composition of TaMoCrTiAl was determined by ICP-OES). The chemical composition of TaMoCrTiAl was taken from [47] and corresponds to the same batch.

alloy	**chemical concentrations $\bar{x}$ of the investigated alloys [at. %]**				
	Ta	**Mo**	**Cr**	**Ti**	**Al**
TaMoCrTiAl	20.1	19.5	19.8	20.4	20.2
TaMoCr10TiAl	22.6	22.4	22.6	10.1	22.3
TaMoCrAl	24.9	25.3	24.8	-	25.0
additional alloy TaCrTi	33.7	-	33.1	33.2	-
additional alloy 20Ta80Cr	20.2	-	79.8	-	-

Samples for the oxidation experiments were taken from the bulk by electrical discharge machining (EDM) and ground to grit P1200. Immediately before the each oxidation experiment, the samples were cleaned in ethanol by ultrasonication. Samples for cross-sectional SEM analyses were ground to P4000 grit using SiC papers, followed by vibratory polishing (2 h with 50 % amplitude) with a 0.1 µm diamond suspension. Oxidation mass change curves were recorded isothermally at 1200 °C with a Rubotherm thermogravimetric system (TGA) in laboratory air. Additional isothermal oxidation tests were performed in a muffle furnace at 1200 °C for 30 min. For XRD analysis, the formed oxide layer of the alloys was first mechanically removed with a scalpel and crushed with a pestle and mortar. Finally, the powder was sieved to a particle size of 40 µm. The diffractograms were recorded on an X'Pert Pro MPD diffraction device equipped with a Cu-Kα tube operated at 45 kV / 40 mA and X-ray detector X`Celerator based on RTMS (real time multiple strip) technology. The scanning was performed in a 2Θ range of 20° – 90° at a step size of 0.005° and a count time of 500 s / step. The lattice parameters were determined using the unit cell lattice parameter refinement module of the PANalytical X`Pert HighScore 4.1 software utilizing default profile fit ($R_{exepected}^2$ / $R_{weighted\ profile}^2$ < 2) and specimen displacement to minimize the influence of systematic errors. Detailed information can be found in Ref. [64]. Cross-sectional microstructural and chemical analysis of the alloys and the oxidized samples were performed with a dual-beam focused ion beam - scanning electron microscope (FIB-SEM) system FEI Helios Nanolab 600 equipped with multiple detectors for backscattered electron (BSE) imaging and EDX. The volume fraction of each phase and the mean thickness of the different oxide layers were evaluated based

on 20 individual BSE measurements images using the software ImageJ. The area fractions of the phases were obtained by binarization of the images. Area and volume fractions are considered equal under the assumption of isotropy and isometry. Site-specific TEM lift-out samples from the oxide layer were prepared using the FEI Helios Nanolab 600 FiB-SEM system through ion milling with Ga^+ ions at acceleration voltages of 5-30 kV depending on the lamella thickness. (Scanning) TEM investigations were performed on a FEI Talos F200X operated at an acceleration voltage of 200 kV. The instrument is equipped with multiple detectors for STEM imaging, a XFEG high-brightness gun, a large-area Super-X EDX detector, and a Gatan Continuum ER spectrometer. The microstructure and chemical composition of the individual oxides were analyzed by high-angle annular dark-field STEM (HAADF-STEM) in combination with STEM-EDX (EDX; k-factors provided in the used software Velox V.3.1.0). Electron energy-loss spectroscopy (EELS) was performed to determine the oxidation states of the cations in the formed oxides (ratio convergence to acceptance angle around 2). To record the Ti-$L_{3,2}$, O-K and Cr-$L_{3,2}$ ionization edges in a single spectrum, the core-loss region was set to 390 - 700 eV at a dispersion of 0.15 eV/channel. The Ta-$M_{5,4}$ and Ta-M_3 ionization edges were recorded in the energy-loss range of 1670 - 2280 eV at 0.3 eV/channel. The low-loss spectra. simultaneously recorded with the respective core losses in dual-EELS-mode, were used to calibrate the energy loss and to determine the relative sample thickness λ / t (λ / t = 0.3 - 0.5 for all TEM lamellae). To record reference spectra for the metal ionization edges the pure oxides, namely TiO_2 (Ti^{4+}) powder (rutile, purity: 99.99 %, metals basis) and Cr_2O_3 (Cr^{3+}) powder (corundum, purity: 99.97 %, metals basis) were purchased from Thermo Fischer GmbH. MaTeck GmbH provided Ta_2O_5 (Ta^{5+}) powder (orthorhombic, purity: 99.99 %). To avoid contamination during the TEM examinations, all samples were cleaned in the Plasma Cleaner NanoClean Model 1070. The values of the standard free enthalpy of the relevant oxides at the temperature of 1200 °C were calculated using the SGPS database of the FactSage V.8 software.

3. Results

3.1 Microstructure

The microstructures of TaMoCrTiAl and TaMoCrAl were already presented in previous publications [45,47,65]. The powder XRD analysis in Fig. 1 of all investigated alloys revealed two phases, namely (i) a C14-type Laves phase (Cr_2Ta) and (ii) an ordered B2-type crystal structure. The B2 super lattice peaks are indicated in addition to the fundamental A2-type peaks by open circles. Only TaMoCrAl contains the additional A15 phase (Mo_3Al; closed square labels). The BSE-SEM images in Fig. 2 illustrate the morphology of the individual phases. The A15 phase is expected to feature the highest intensity due to the high content of Mo, while a medium intensity is anticipated for the Laves phase Cr_2Ta. TaMoCrTiAl consists of large B2 grains. Along the grain boundaries, the Laves phase is precipitated. The Laves phase volume fraction was reported earlier to be 0.4 vol. % [47]. Reducing the Ti content to 10 at. % (TaMoCr10TiAl) results in a two-phase microstructure of B2 phase and Laves phase; the volume fractions are approximately 68 vol. % and 32 vol. %, respectively. TaMoCrAl possesses a three-phase microstructure after heat treatment, containing Laves phase C14 in addition to B2 and A15 [45]. Laves phase C14 predominates in this alloy with about 65 vol. % [45]. At higher magnification, the A15 phase (bright contrast) and the B2 phase (dark contrast) are identified in Fig. 2 d.

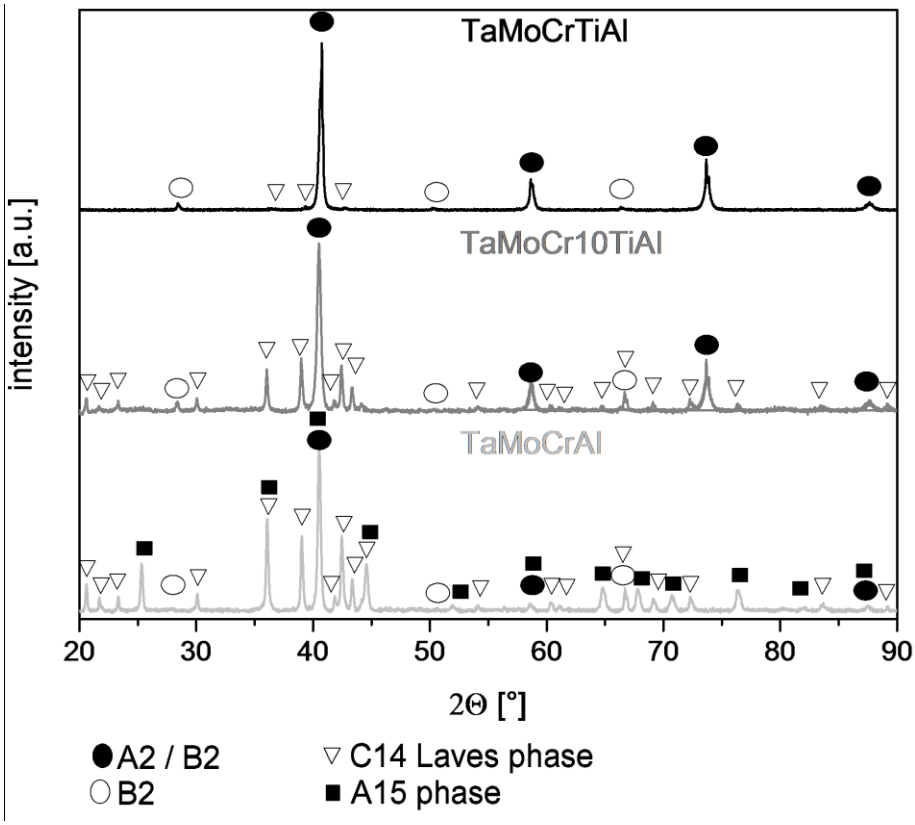

Fig. 1 Powder XRD pattern of the investigated alloys after homogenization at 1500 °C for 20 h. Closed circles indicate A2 / B2 Bragg peaks; open circles highlight visible B2 Bragg peaks. TaMoCrTiAl and TaMoCrAl correspond to the samples investigated in [45]. The peaks are labeled according to simulated XRD data based on the structures listed in the legend.

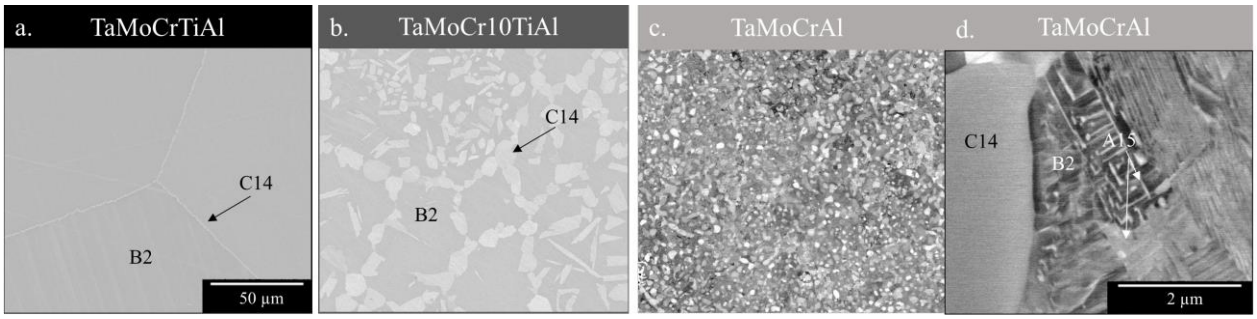

Fig. 2 BSE-SEM micrographs of the investigated alloys after homogenization 1500 °C / 20h: a. TaMoCrTiAl, b. TaMoCr10TiAl, c. TaMoCrAl, d. BSE-SEM image of the TaMoCrAl at higher magnification. All BSE-SEM micrographs, except image d., were taken at the same magnification.

3.2 Oxidation kinetics

Fig. 3 represents the specific mass changes as a function of time for the alloys with varying Ti contents during isothermal exposure to air at 1200 °C. The mass change curve of TaMoCrTiAl is taken from [47]. The oxidation kinetics of TaMoCrTiAl obeys a parabolic rate law [47]. The recorded mass gain at a temperature of 1200 after 24 h °C is 5.29 mg/cm² [47]. In comparison to TaMoCrTiAl, TaMoCr10TiAl exhibits a slightly higher mass change over the entire test time. After 24 h oxidation, TaMoCr10TiAl reveals a mass change of 6.19 mg/cm². In contrast, the Ti-free alloy displays significantly lower initial kinetics, followed by an increasingly pronounced mass loss over time.

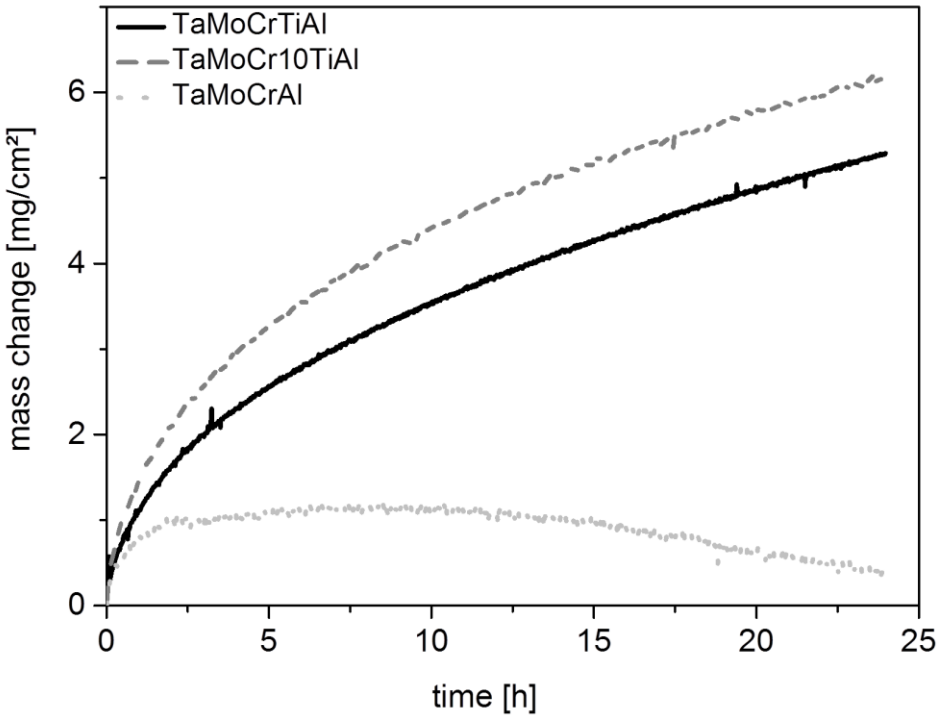

Fig. 3 Specific mass change as a function of time for investigated alloys during isothermal exposure to air at 1200 °C. The mass change curve of TaMoCrTiAl is taken from [47].

3.3 Crystallographic analysis of the oxide products

In Fig. 4, the XRD results of the oxides after oxidation at 1200 °C for 24 h are presented. The diffraction pattern of the oxide products on TaMoCrTiAl reveals Al_2O_3, Cr_2O_3, TiO_2 and a further rutile-type oxide based on the $CrTaO_4$ crystal structure [47]. The rutile-type oxide is referred to as rutile Cr-Ta-(Ti) oxide in the subsequent part of the results. The XRD measurement of TaMoCr10TiAl after oxidation indicates the presence of the same oxides. For the oxidized TaMoCrAl, no TiO_2 but Ta_2O_5 oxide was detected. In addition, the crystal structure of the oxides formed on the additional alloys TaCrTi and 20Ta80Cr was investigated by XRD. The respective diffraction patterns are given in the supplementary material Fig S. 1. While Ta_2O_5, Cr_2O_3, TiO_2 and rutile Cr-Ta-(Ti) oxide were found on the additional alloy TaCrTi, Cr_2O_3 and a rutile Cr-Ta oxide were identified on 20Ta80Cr. Table 2 reports the lattice parameters of rutile Cr-Ta-(Ti) oxide, which were derived from the XRD data in Fig. 4.

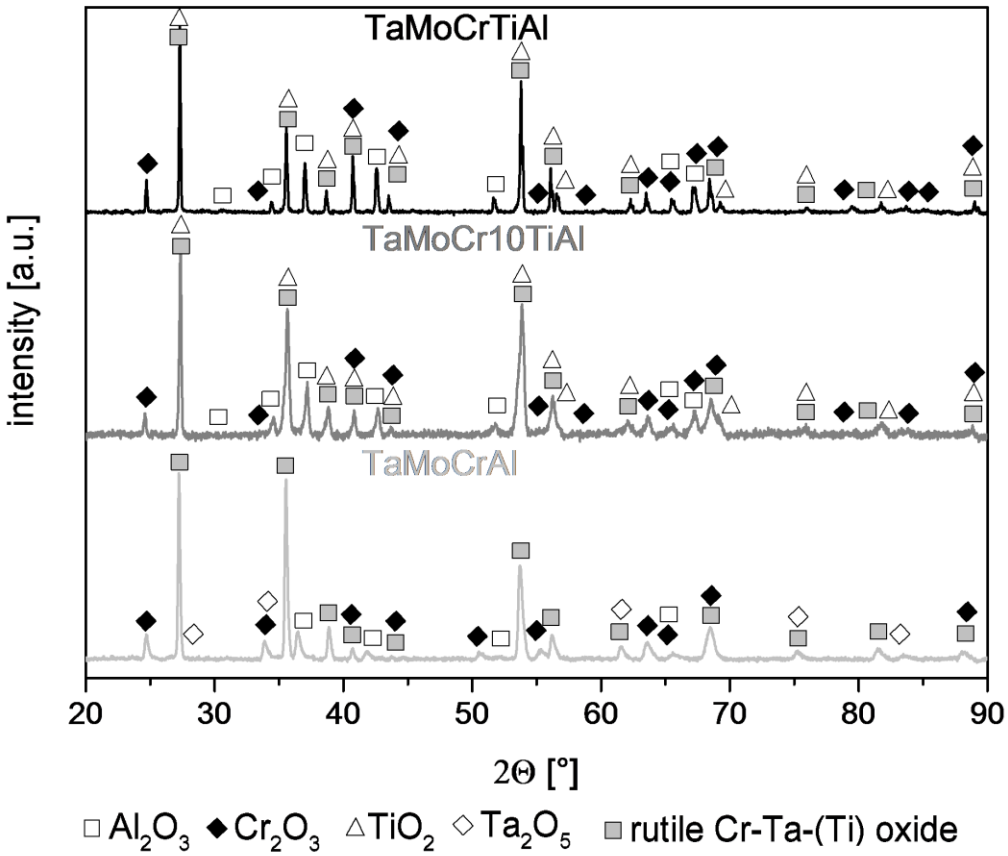

Fig. 4 XRD pattern of investigated alloys oxidation at 1200 °C for 24 h in air. The diffraction pattern of TaMoCrTiAl is taken from [47]. The peaks are labeled according to simulated XRD data based on the structures of the oxides listed in the legend.

Table 2 Determined lattice parameters from XRD measurements of rutile Cr-Ta-(Ti) oxide after oxidation at 1200 °C for 24 h. The lattice parameter of rutile Cr-Ta-Ti oxide formed on TaMoCrTiAl is taken from [47].

alloy	rutile Ta-Cr-(Ti) oxide lattice parameter	
	a [Å]	c [Å]
TaMoCrTiAl [47]	4.635	3.011
TaMoCr10TiAl	4.637	3.013
TaMoCrAl	4.642	3.018
additional alloy TaCrTi	4.634	3.007
additional alloy 20Ta80Cr	4.643	3.019

3.4. Microstructural analysis of oxide scales

After the oxidation tests, macroscopic images of the samples were taken (Fig. 5). All samples display an intact oxide outer scale, no cracks or flaking are visible. Cross-sectional BSE-SEM images of the oxide layers oxidation to air at 1200 °C for 24 h are depicted in Fig. 6. In all cases complex multi-layer oxide structures are visible. A multilayered oxide scale consisting of outer TiO_2, Al_2O_3, Cr_2O_3 and inner rutile Cr-Ta-Ti oxide layer as well as an underlying distinct zone of internal corrosion was reported in our previous studies for TaMoCrTiAl oxidized under the same conditions [46,47]. Using a marker experiment, it was established that the rutile Cr-Ta-Ti oxide layer at the oxide/substrate interface grows inwards as a result of oxygen inward diffusion [47]. Beneath the Cr-Ta-Ti oxide layer, a distinct zone of internal corrosion with Al_2O_3 and TiN particles is formed [47]. In the present work, by combining XRD and SEM-EDX (SEM-EDX-mapping Fig S. 2), the same multilayered oxide structure was identified for oxidized TaMoCr10TiAl. Noticeable decoration of the phase boundaries in the internal corrosion zone by Al_2O_3 and TiN particles was observed (see also Fig S. 2 detail image of the dashed frame in Fig. 6 b.). Due to the absence of Ti in TaMoCrAl, no TiO_2 is formed and, instead, a thin semi-continuous outermost layer of Cr_2O_3 and

underlying Al_2O_3 particles is formed (Fig. 6 c.). Beneath, a thick and porous inner layer consisting of a mixture of rutile Cr-Ta oxide, Ta_2O_5, Al_2O_3 and Cr_2O_3 is observed. Below this, a zone of internal corrosion with Al_2O_3 and Cr_2N particles is present. The formed oxide scale on the alloy TaMoCrAl is in accordance with the investigations of Müller et al. [45] after oxidation at 1000 °C for 48 h. In the supplementary material (Fig S. 3), the EDX mapping of the alloy TaMoCrAl after oxidation is depicted. Furthermore, detailed images in higher magnification of the outer oxide layers formed one TaMoCr10TiAl and TaMoCrAl are provided in supplementary material Fig S. 4 and Fig S. 5, respectively.

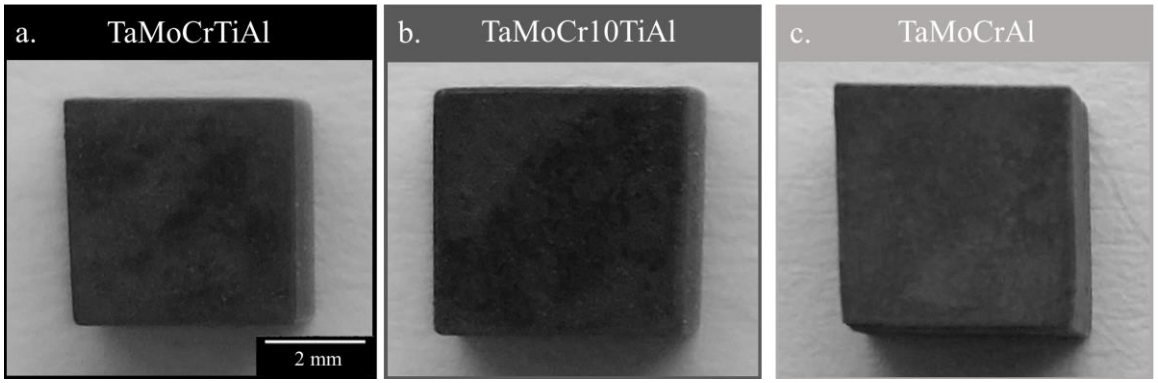

Fig. 5. Makrsopic images of oxidized samples after exposure to air at 1200 °C for 24 h: a. TaMoCrTiAl, b. TaMoCr10TiAl, c. TaMoCrAl.

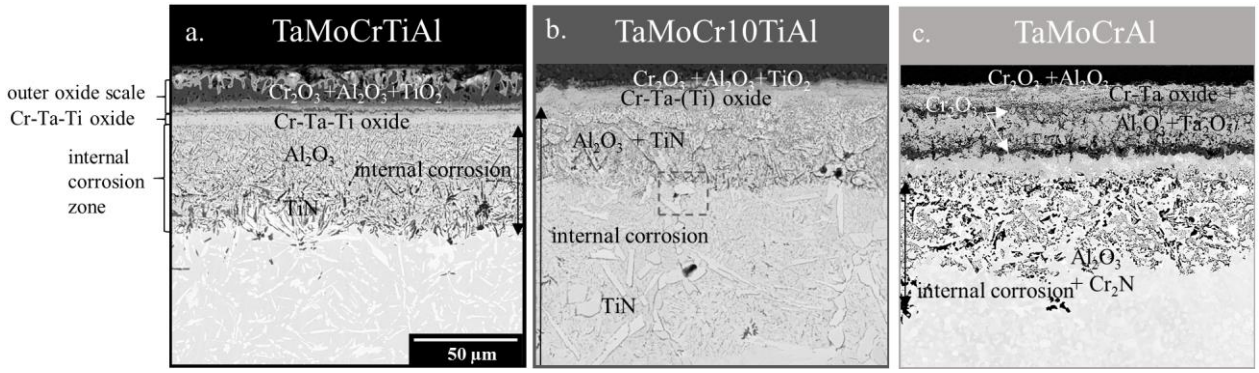

Fig. 6. BSE-SEM images of investigated alloys after exposure to air at 1200 °C for 24 h. Detail image of the dashed frame in b. is presented in Fig S. 3. In addition, detailed images of the outer oxide layers of b. and c. are given in Fig. 2 and Fig. 3.

Fig. 7 quantitatively represents the measured thicknesses of the outer oxide layer, the rutile Cr-Ta-(Ti) oxide layer at the oxide/substrate interface and the underlying internal corrosion zone. The outer oxide layer consists of Cr_2O_3, Al_2O_3 and TiO_2 for TaMoCrTiAl as well as TaMoCr10TiAl and Cr_2O_3, Al_2O_3 for TaMoCrAl. The thickness of the rutile Cr-Ta-(Ti) oxide scale increases with reduced Ti content. In the case of the Ti-free alloy, the rutile Cr-Ta oxide scale is more pronounced in comparison to the zone of internal corrosion. The alloy with 10 at.%Ti yields the thickest zone of internal corrosion, while the Ti-free alloy possesses the thinnest one.

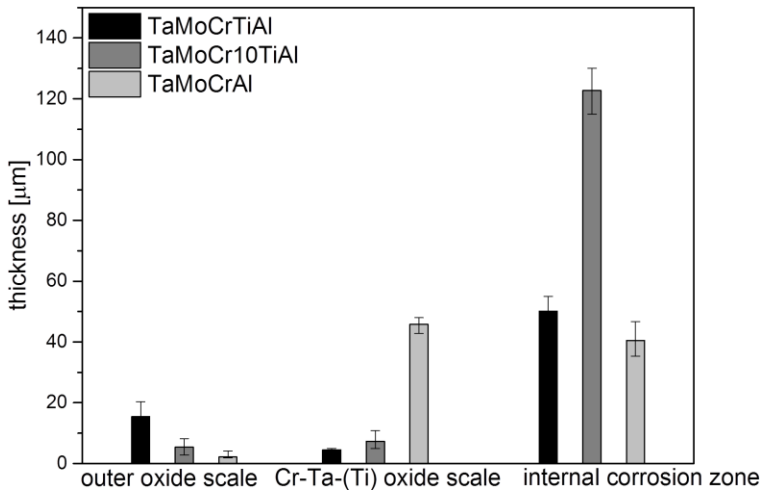

Fig. 7 Thicknesses of outer oxide scale, Cr-Ta-(Ti) oxide scale and internal corrosion zone on investigated alloys after oxidation at 1200 °C for 24 h.

To investigate the rutile Cr-Ta-(Ti) oxide scales in more detail, site-specific TEM lamellae were extracted from the oxidized samples. In Fig. 8 HAADF-STEM images are depicted together with the corresponding chemical maps by STEM. Furthermore, the "X-marks" indicate the locations where EELS spectra (Fig. 10.) were recorded for detailed chemical-bond analyses. Below the TiO_2 scales, a network of Cr_2O_3 particles is visible in the TaMoCrTiAl (Fig. 8 a.). In the scale of TaMoCr10TiAl, however, only a few isolated Cr_2O_3 particles with an average diameter of approximately 400 nm are detected (Fig. 7 b.). Above the metallic substrate, the rutile Cr-Ta-(Ti) oxide scales (highlighted by blue frames) consisting of the elements Ta, Ti, Cr and O are identified on both alloys with Ti. The FIB lamella of TaMoCrAl alloy was extracted from the centre of the rutile Cr-Ta oxide scale because the alloy forms a thick oxide layer. In Fig. 8 c., a mixture of rutile Cr-Ta oxides and Al_2O_3 particles is observed. In addition, the STEM-EDX mappings prove the absence of Mo in the oxide layers.

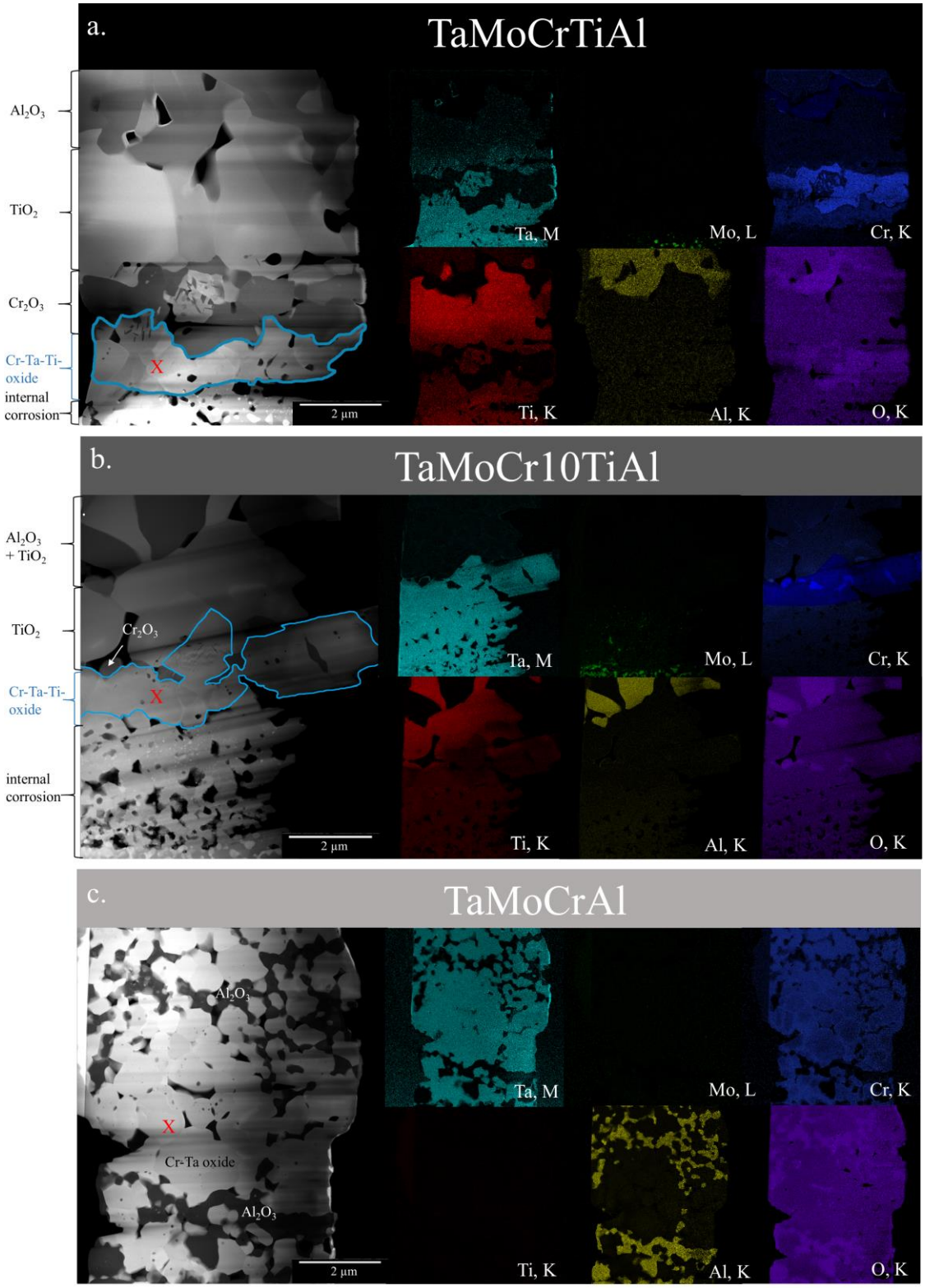

Fig. 8 HAADF-STEM micrographs with corresponding EDX mappings of extracted TEM lamellae form rutile Cr-Ta-(Ti) oxide scales of the investigated alloys after oxidation to air at 1200 °C for 24 h: a. TaMoCrTiAl, b. TaMoCr10TiAl and c. TaMoCrAl. "X" marks the location of the EELS records. Micrographs a. of TaMoCrTiAl taken from [47].

The STEM-EDX results were quantified to determine the relative metal concentrations in the formed rutile Cr-Ta-(Ti) oxides (Fig. 9). All oxides, regardless of the Ti content in the alloys, correspond to a MeO_2 stoichiometry. However, the ratio of the metallic elements Me = Ti, Ta and Cr in the formed rutile Cr-Ta-(Ti) oxides varies. A higher amount of Ti and a lower concentration of Cr were measured in rutile Cr-Ta-Ti oxide formed on TaMoCrTiAl. The opposite observations were made in the case of the alloy with 10 % Ti. In rutile Cr-Ta oxide on TaMoCrAl, equal amounts of Cr and Ta were found.

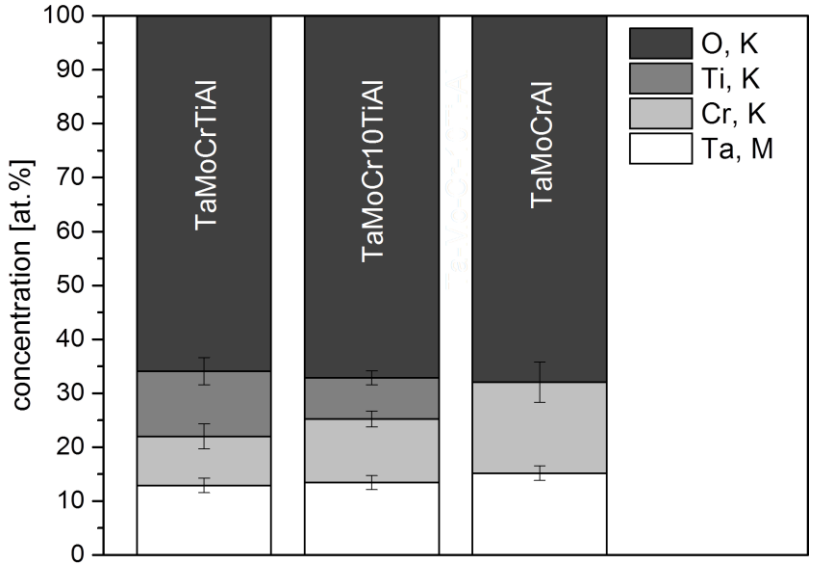

Fig. 9 Element distribution [at. %] in the rutile Cr-Ta-(Ti) oxides of the TEM lamellae in Fig. 8 (blue frame in a. and b., Al depleted region in c). The elemental distribution was determined from the STEM-EDX mappings by quantification of integrated spectral intensities from homogeneous regions of the Cr-Ta-(Ti) oxides.

In literature, the following chemical reaction for the formation of $CrTaO_4$ corresponding to a solid solution oxide of the stoichiometry $2(Cr,Ta)O_2$ with Cr, Ta evenly distributed of the cation sites of rutile crystal structure is known [45,66–68]:

$$\frac{1}{2}Cr_2O_3 + \frac{1}{2}Ta_2O_5 \rightarrow CrTaO_4 \tag{1}$$

The formation of the Ti-containing $CrTaTiO_6$ corresponding to a solid solution $3(Cr,Ta,Ti)O_2$ oxides was postulated as follows [69]:

$$\frac{1}{2}Cr_2O_3 + \frac{1}{2}Ta_2O_5 + TiO_2 \rightarrow CrTaTiO_6 \tag{2}$$

Assuming charge neutrality of the compounds and ~~an~~ unequivocal oxidation of O^{2-}, the following oxidation states of the metallic elements in the oxides of equations (1) & (2) are obtained: Cr^{3+}, Ta^{5+}, and Ti^{4+}. To verify this postulation, the EELS near-edge structures of the L/Mionization edges of the different cations were analyzed, which reflect the respective oxidation states in terms of the edge shape and onset. Specifically, spectra of the L edges of Ti and Cr, the O-K edge and the Ta-M edge of the rutile Ta-Cr-(Ti) oxides, formed on the different alloys, were recorded on the respective TEM lamellae at the positions as labeled in Fig. 8 and Fig S. 7. The oxidation states of the formed rutile Cr-Ta-(Ti) oxides on the RHEAs were identified by comparison with reference spectra of pure TiO_2, Cr_2O_3 and Ta_2O_5 reference particles (cf. equations (1) and (2)). In addition, EELS of the formed oxides on the additional alloys 20Ta80Cr ($CrTaO_4$ former) and TaCrTi ($CrTaTiO_6$ former) was performed. The extraction locations of the TEM lamellae of the formed rutile Cr-Ta-(Ti) oxides on the additional alloys are displayed in Fig S. 6. Fig S. 7 represents the TEM lamellae of those oxides. The identity of the reference materials was verified by XRD patterns and HAADF-STEM images which are given in supplementary material (Fig S. 8 and Fig S. 9). All EELS spectra are summarized in Fig. 10.

In terms of both, the shape of the edges as well as their onset energy, all metal edges are in excellent agreement with their respective references and verify the oxidation states initially derived from (1) and (2), i.e. the rutile (Cr,Ta,(Ti))O_2 oxides consist of Ta^{5+}, Cr^{3+} and Ti^{4+}. For all oxides containing Ti (rutile (Cr,Ta,Ti)O_2 oxides) and the TiO_2 references the Ti-L_3 and Ti-L_2 edges are observed at 456 eV and 462 eV, respectively. The two edges show double-peak shape at the same energy loss, which is typical of Ti^{4+} coordinated by O^{2-} [59]. Similarly, the Cr-L_3 and Cr-L_2 edges of all Cr containing oxides rutile (Cr,Ta,(Ti))O_2 oxides and the Cr_2O_3 reference are observed at 575 eV and 584 eV, respectively [70]. As for the Ti and Cr, the Ta-M edges in the EELS of the oxides rutile (Cr,Ta,(Ti))O_2 oxides and the Ta_2O_5 reference are remarkably similar as the shape of the edges are nearly identical and the individual edges appear at the same energies (1735 eV, 1793 eV and 2194 eV for the Ta-M_5, Ta-M_4 and Ta-M_3 edge, respectively) [71]. The O-K edge cannot directly be compared to the reference spectra as the O-K edge (532 eV) is very sensitive to the metal cations in the coordination sphere of each O^{2-} anion.

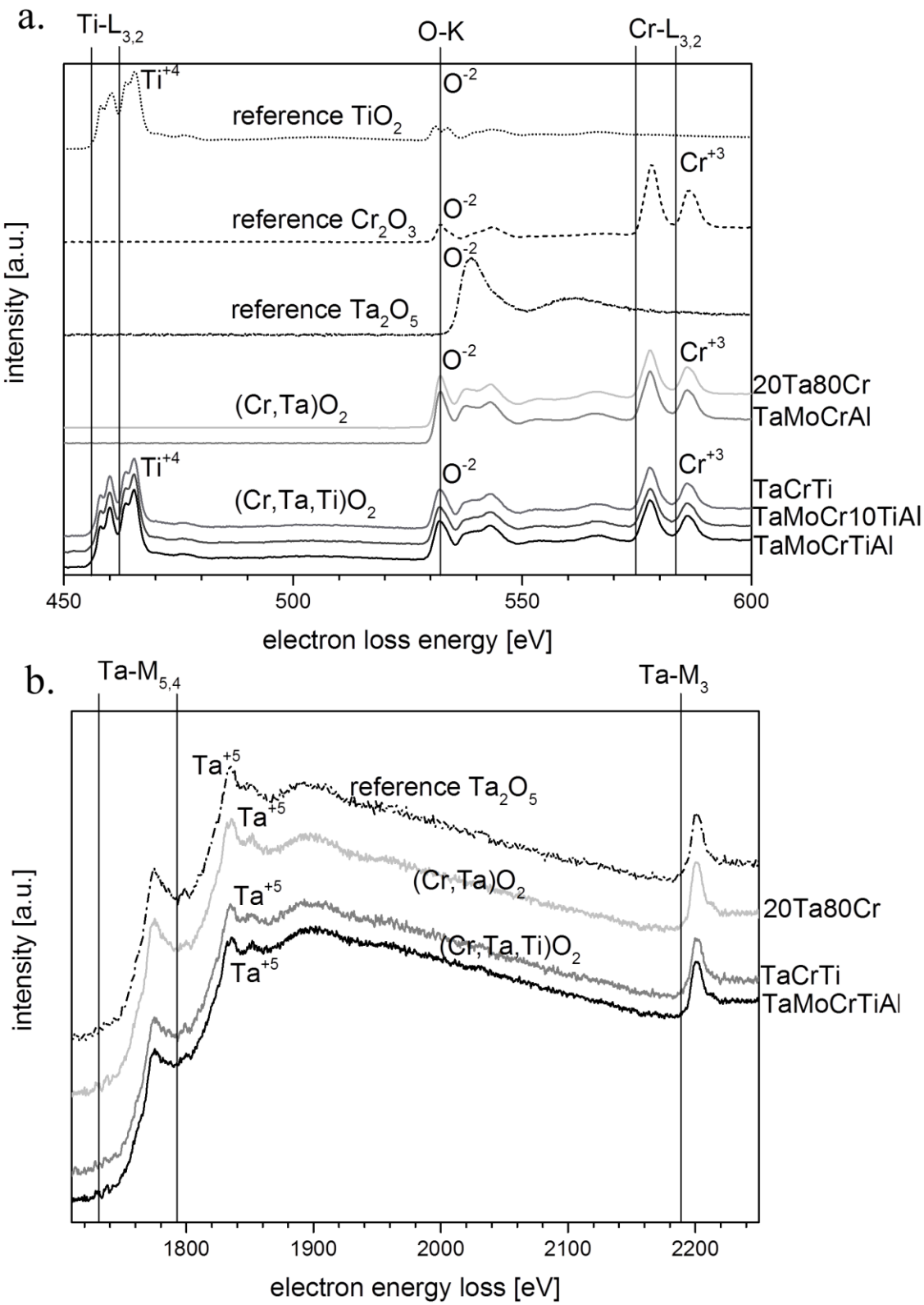

Fig. 10 a. EEL spectra of the energy-loss range 450 - 600 eV (Ti-L, O-K, Cr-L edges) of the reference materials TiO_2, Cr_2O_3 and Ta_2O_5 in dotted lines and the formed oxides on the investigated alloys presented in Figure 8. b. Ta-M edges (energy-loss range 1700 - 2250 eV) of the reference material Ta_2O_5, the rutile $(Cr,Ta)O_2$ of the additional alloy 20Ta80Cr, as well as the rutile $(Cr,Ta,Ti)O_2$ of the additional alloy TaCrTi and TaMoCrTiAl. The spectra of the Ta-M edges are identical for the rutile $(Cr,Ta)O_2$ of TaMoCrAl and rutile $(Cr,Ta,Ti)O_2$ TaMoCr10TiAl and not shown here.

4. Discussion

Compared to the Ti-containing rutile $(Cr,Ta,Ti)O_2$ forming alloys, the TaMoCrAl reveals a significantly thicker and porous oxide layer. In preliminary studies, Müller et al. [45] postulated that the higher Mo content in TaMoCrAl and the higher content of non-oxidation-resistant A15 phase (Mo_3Al) [72] of this alloy dramatically deteriorate the oxidation behaviour at 1000 °C. Mo is well-known to create volatile MoO_3 above 800 °C [25,73,74]. This gaseous oxide evolves also during the oxidation of the A15 phase and results in pores¸ which create new surfaces and further accelerate the oxidation and evaporation of Mo [45]. Furthermore, the authors reported the formation of Ta_2O_5 in the oxide layer that causes growth stresses leading to the formation of cracks and partial flaking of the oxide layer [45]. The oxidation behaviour of this alloy at 1200°C is similar to that observed at 1000°C [22]. A negative mass change was detected (Fig. 3). The porous oxide scale consists of a mixture of Al_2O_3 particles and rutile $(Cr,Ta)O_2$ after oxidation at 1200 °C for 24 h. The chemical compositions as well as the morphology of the two regions in the TEM lamella indicate that the Cr_2Ta Laves phase forms rutile $(Cr,Ta)O_2$ whereas the Al_2O_3 particles originate from the oxidized A15 phase.

The experimental results in this study reveal that the chemical nature of the rutile $(Cr,Ta,Ti)O_2$ changes with varying Ti content in the alloy system. The characteristics of these complex rutile oxides differ enormously. For example, Li et al. [75] found that the compact Al_2O_3 on the surface of the alloy Ta-10W-6Al (wt.%) is consumed during oxidation at 1000 °C (4 h) as a result of rutile $AlTaO_4$ scale formation and, consequently, a mesh-type structure is formed, which does not effectively protect the substrate. In line with this finding, Mitsui et al. [76] observed the formation of a thick oxide layer consisting of a mixture of α-Al_2O_3, β-Ta_2O_5 and rutile $AlTaO_4$ after oxidation of the sputter-deposited Al-80Ta (at. %) alloy at 900 °C (p_{O2}=20 kPa) for 20 h. A positive effect of rutile $TiTaO_4$ on chromium oxide forming Ni-based superalloys is reported by Jalowicka et al. [77]. They demonstrated that the formation of rutile $TiTaO_4$ particles prevents the incorporation of Ti into the protective Cr_2O_3 scale and, thus, enhances the oxidation resistance of Ni-based superalloy PWA1483 as well as various Ta- and Ti-containing model alloys in synthetic air at 1050 °C up to 500 h. Comparing the oxidation behaviour of Rene 80 and IN 792 at 1050 °C in Ar-20 % O_2 up to 50 h, Nowak et al. [78] concluded that the formation of rutile $TiTaO_4$ prevents the Ti flux to the outer interface and reduces the oxidation kinetics. It should be noted that rutile $TaTiO_4$ forms underneath the protective scale and only serves as a barrier for Ti outward diffusion. In contrast to rutile $TaTiO_4$, a clear protective effect of continuous rutile $CrTaO_4$ layers at the substrate/oxide interface on nickel-based superalloys is reported [66,79,80]. Ren et al. observed that the continuous rutile $CrTaO_4$ layer inhibits the outward diffusion of cations on the one hand and reduces the inward diffusion of oxygen on the other hand on a directionally-solidified nickel-based superalloy with 5.0 wt. % Ta during oxidation at temperatures between 850 and 900 °C for up to 300 h [66]. Lo et al. also reported such a protective effect of rutile $CrTaO_4$ on the RHEA 13.4Ta15.2Nb20.3Mo25.2Cr5.4Ti17.6Al2.9Si (at. %), during oxidation at 1000 °C and 1100 °C for 200 h [55]. The EDX measurements in this study revealed that there are considerable amounts of other elements dissolved in the rutile $CrTaO_4$ (7 at.% Al, 0.2 at.% Si, 3.9 at.% Ti, 6.3 at.% Nb, and 2.8 at.% Mo), which explain the different lattice parameters compared to pure rutile $CrTaO_4$. Mani et al. published the lattice parameters in addition to the electrical properties of rutile $AlTaTiO_6$ and rutile $CrTaTiO_6$ [69,81]. Peterson et al. and Mani et al. pointed out that rutile $CrTaTiO_6$ undergoes cell distortion towards higher lattice parameters compared to rutile TiO_2 due to the larger average interatomic distances between the cations as well as the cations and anions as a result of the different ionic radii [69,81,82]. However, the axial ratios are similar to those of rutile TiO_2 [69,81]. About comprehensive study on the protective properties of complex rutile oxides based on Ta, Ti (and Cr) at high temperatures is not reported in literature.

In Fig. 11, literature data on lattice parameters of various complex rutile oxides ($AlTaO_4$ [83,84], $AlTaTiO_6$ [69], $CrTaO_4$ [81,82,85], $CrTaTiO_6$ [69], $TaTiO_4$ [82,85,86]) and rutile TiO_2 [87–90] are compared with the determined lattice parameters of the formed rutile $(Cr,Ta,Ti)O_2$ on the investigated alloys (see Table 2). Additionally, lattice parameters of the rutile $CrTaO_4$ formed on RHEA 13.4Ta15.2Nb20.3Mo25.2Cr5.4Ti17.6Al2.9Si (in at. %) during oxidation at 1000 °C and 1100 °C for 200h are also included [26]. The determined lattice parameters of the rutile $(Cr,Ta)O_2$ formed on TaMoCrAl (a = 4.642 Å, c = 3.018 Å) and the additional alloy 20Ta80Cr (a = 4.643 Å, c = 3.019 Å) are similar to those reported in literature for rutile $CrTaO_4$ [81,82,85,91]. In addition to the similarity in lattice parameters, the local compositions as derived from STEM-EDX (Fig. 9 and Fig. 10) are in agreement with the chemical composition of the formed rutile $(Cr,Ta)O_2$. The determined lattice parameters of rutile $(Cr,Ta,Ti)O_2$ grown on the TaMoCrTiAl (a = 4.635 Å, c = 3.011 Å) [47] are elongated in both, a and c direction compared to rutile $CrTaTiO_6$ (a = 4.633 Å, c = 3.003 Å) by 0.04 % and 0.27 %, respectively. Thus, they lie between the parameters of rutile $CrTaO_4$ and rutile $CrTaTiO_6$ [69,81,82,85,91]. The lattice parameters of the formed rutile $(Cr,Ta,Ti)O_2$ on

TaMoCr10TiAl and TaCrTi are close to those of the oxide grown on TaMoCrTiAl (Fig. 11). Combining the knowledge about the lattice parameters and the TEM-EELS results (Fig. 10) it is concluded that the type rutile $(Cr,Ta,Ti)O_2$ forms on TaCrTi, TaMoCr10TiAl and TaMoCrTiAl. The lattice parameters of the rutile $(Cr,Ta,Ti)O_2$ formed on TaCrTi are slightly shifted towards rutile $CrTaTiO_6$, whereas the lattice parameters of the rutile $(Cr,Ta,Ti)O_2$ of the alloy TaMoCr10TiAl are slightly stretched towards rutile $CrTaO_4$ compared to the parameters of rutile $(Cr,Ta,Ti)O_2$ grown on TaMoCrTiAl. It should be noted in this context that only a single lattice parameter dataset of rutile $CrTaTiO_6$ exists in literature. The increased lattice parameter of rutile $(Cr,Ta,Ti)O_2$ formed on TaMoCr10TiAl compared to that of TaMoCrTiAl could be explained by the slightly higher Ta content and the depletion of the element Ti with the smallest ionic radius in the non-stoichiometric rutile $(Cr,Ta,Ti)O_2$ (Fig. 9). This presumption is supported by the larger lattice parameter of the rutile $(Cr,Ta)O_2$ of TaMoCrAl with an even higher Ta content (cf. Fig. 9).

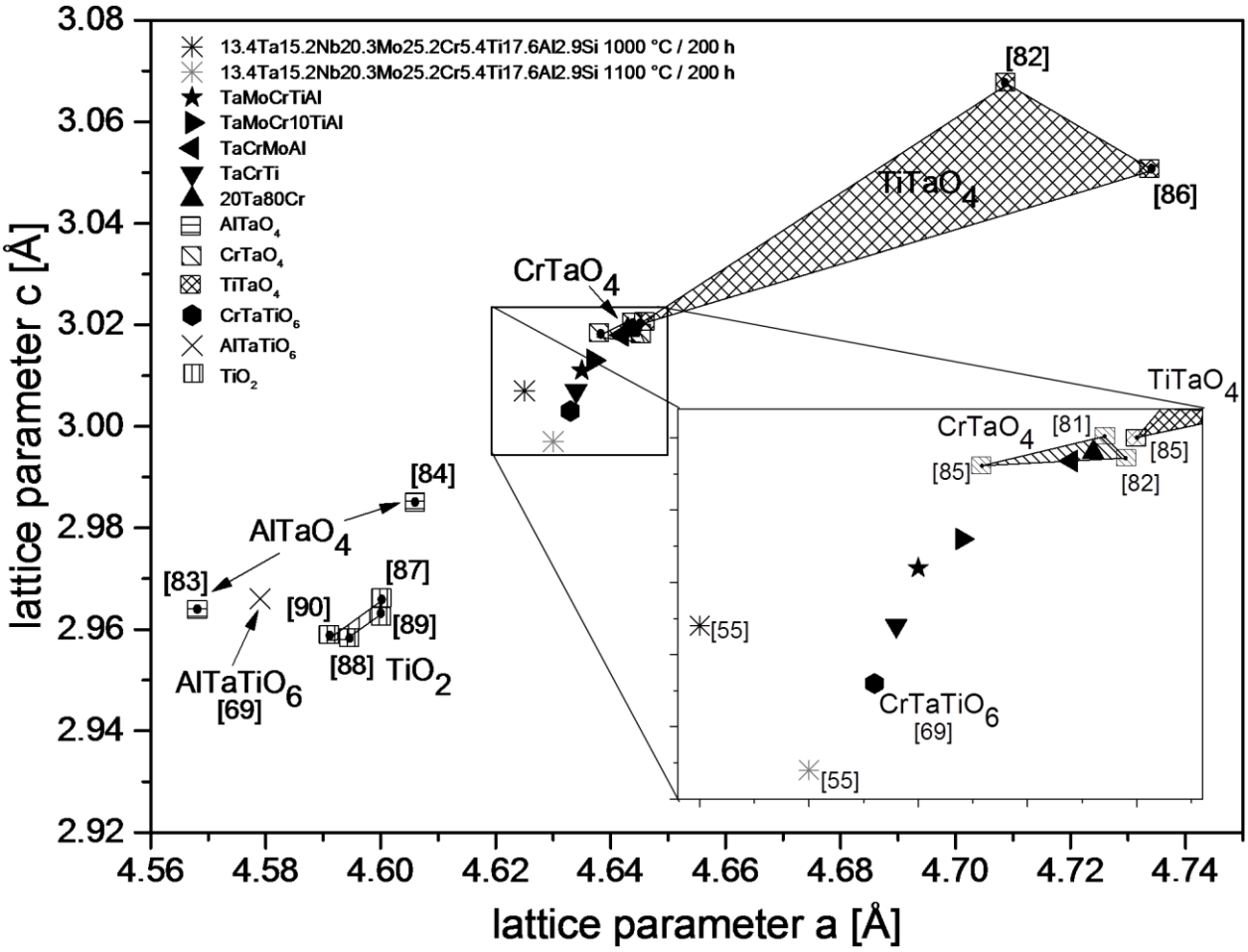

Fig. 11 Literature data on lattice parameters of various complex rutile oxides ($AlTaO_4$, $AlTaTiO_6$, $CrTaO_4$, $CrTaTiO_6$, $TaTiO_4$) and lattice parameters of rutile $(Cr,Ta,(Ti))O_2$ formed on the alloys (TaMoCrTiAl, TaMoCr10TiAl, TaMoCrAl, 20Cr80Cr, TaCrTi) after 24 h oxidation at 1200 °C in air. In addition, lattice parameters of rutile $CrTaO_4$ oxide on RHEA 13.4Ta15.2Nb20.3Mo25.2Cr5.4Ti17.6Al2.9Si (at. %) after oxidation to air at 1000 °C and 1100 °C for 200 h are given.

Previous studies revealed that the protective rutile $(Cr,Ta,Ti)O_2$ formed on the TaMoCrTiAl alloy grows in a parabolic manner inwards at the metal-oxide interface due to oxygen diffusion. [45,47]. The valence states according to the TEM-EELS results (Fig. 10) of an idealized rutile $(Cr,Ta,Ti)O_2$ are Cr^{3+}, Ti^{4+}, Ta^{5+} with an oxidation state of O of 2-. As EELS indicates, no significant concentrations of metal ions of differing oxidation states were observed. Fig. 12 illustrates the hypothetically ideal lattice of rutile $(Cr,Ta,Ti)O_2$ and the possible oxygen vacancy formation with the corresponding defect formula (equation (3)). As equation 3 illustrates, it is assumed that the rutile $(Cr,Ta,Ti)O_2$ grows by oxygen diffusion through vacancies in the anion sublattice.

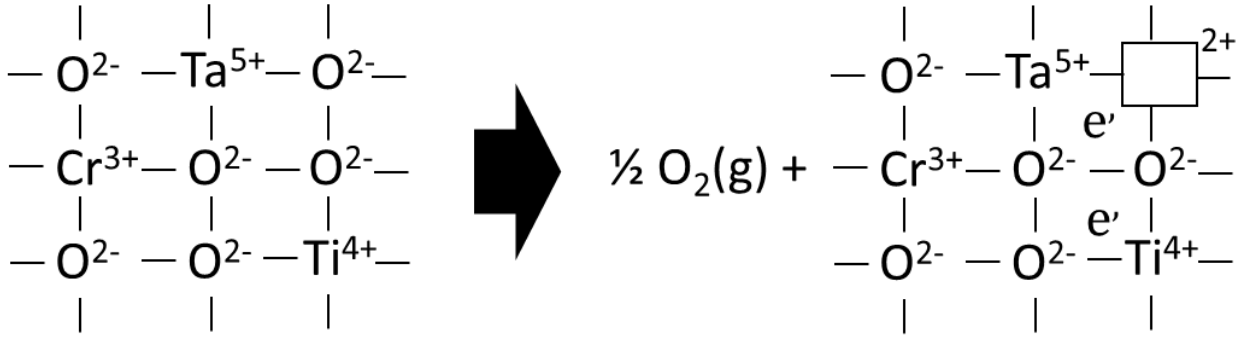

Fig. 12 Ideal atomic lattice of rutile (Cr,Ta,Ti)O_2 and formation of a vacancy in a n-type semi-conducter oxide.

$$O_O^x = 2e' + \frac{1}{2}O_{2(g)} + V_O^{\bullet\bullet} \tag{3}$$

The chemical analysis in Fig. 9 discloses a non-equimolar ratio of the cations (Cr, Ta, Ti) in the formed (Cr,Ta,Ti)O_2 on the alloys with different Ti contents (TaMoCrTiAl and TaMoCr10TiAl). Apparently, the Ta contents are nearly the same indicating that Ti tends to occupy the Cr sites. The following defect equation is formulated:

$$V_O^{\bullet\bullet} + Cr_{Cr} + TiO_2 = Ti_{Cr}^{\bullet} + O_O + Cr_i^{\bullet\bullet\bullet} + \frac{1}{2}O_2 + 2e' \tag{4}$$

Classical oxidation theory states that occupation of cation sites by higher valence cations causes a decreased concentration of $V_O^{\bullet\bullet}$ in n-type conducting oxides and results in a reduced growth rate of the oxide. By comparing the resulting oxide layers on TaMoCr10TiAl and TaMoCrTiAl, a positive impact on the oxidation behaviour with increasing Ti content is revealed, which can be attributed to the replacement of Cr^{3+} by Ti^{4+} on the cationic sublattice. The following experimental results support the assumption of defect equation (4): (i) According to equation (4), the occupation of Cr^{3+} cation lattice sites by Ti^{4+} reduces the vacancy concentration in the oxide, which implies a thinner and less permeable rutile (Cr,Ta,Ti)O_2 scale. As shown in Fig. 7, the alloy with a higher Ti content (TaMoCrTiAl) forms a thinner rutile (Cr,Ta,Ti)O_2 layer and less pronounced zone of internal corrosion with Al_2O_3 and TiN precipitates in comparison to TaMoCr10TiAl. (ii) Equation (4) discloses that, if Ti^{4+} cations occupy Cr^{3+} cation lattice sites, Cr must adopt interstitial lattice sites. The interstitial Cr can further diffuse outwards and react with O^{2-} to Cr_2O_3. As a consequence, the rutile (Cr,Ta,Ti)O_2 would become Cr-depleted and more Cr_2O_3 particles would be formed in the vicinity of (Cr,Ta,Ti)O_2. The EDX analysis reveals (Fig. 9), on the one hand, a higher Ti content and, on the other hand, a reduced Cr content in the formed rutile (Cr,Ta,Ti)O_2 on TaMoCrTiAl as compared to TaMoCr10TiAl. Moreover, the higher content of released Cr in TaMoCrTiAl seems to react with oxygen forming a nearly continuous chromia scale (see Fig. 8. a.), while only a few chromia particles were found above the (Cr,Ta,Ti)O_2 scale (see Fig. 8. b.).

Finally, the free standard enthalpies of formation ΔG of the relevant oxides in the Ta-Mo-Cr-Ti-Al system were calculated at 1200 °C using the software FactSage. The calculations of ΔG of the complex rutile oxides are based on the chemical reactions given in equations (1) and (2) and are as follows:

$$\Delta G_{CrTaO4}^0 = \frac{1}{2}(\Delta G_{Cr2O3}^0 + \Delta G_{Ta2O5}^0) \tag{5}$$

$$\Delta G_{CrTaTiO6}^0 = \frac{1}{2}(\Delta G_{Cr2O3}^0 + \Delta G_{Ta2O5}^0) + \Delta G_{TiO2}^0 \tag{6}$$

The calculated free standard enthalpies of formation of the relevant oxides are displayed in Fig. 13. From a thermodynamic point of view, a chemical reaction as described in equation (2) to $CrTaTiO_6$ (corresponds to (Cr,Ta,Ti)O_2) involving the oxide TiO_2, which has a lower standard free enthalpy of formation (-676 kJ / mol O_2) compared to the oxide $CrTaO_4$ (corresponds to (Cr,Ta)O_2) (-535 kJ / mol O_2), results in a higher thermodynamic driving force of formation (-606 kJ / mol O_2). The high thermodynamic stability of $CrTaTiO_6$ (i.e. higher than that of chromia) in addition to the low growth rate (i.e. lower than that of chromia [58]) reveal attractive protective properties. It should, however, be stressed that similar to chromia $CrTaTiO_6$ suffers from high diffusion rates of oxygen and nitrogen resulting in thick zones of internal corrosion (see Fig. 6).

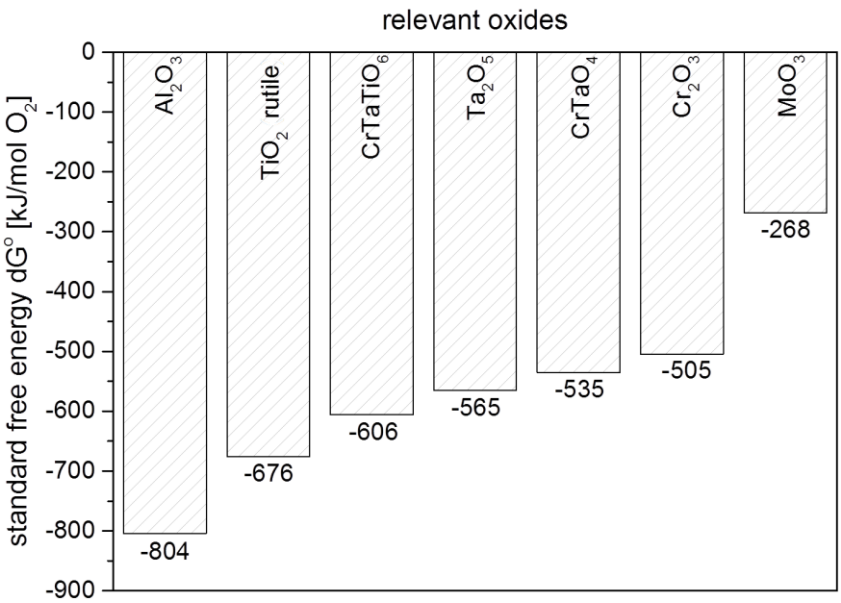

Fig. 13 Calculated standard free energy of formation of relevant oxides at 1200 °C.

5. Conclusions

Rutile (Cr,Ta,Ti)O_2 with a non-stoichiometric ratio of metallic elements Me = Ti, Ta and Cr form on RHEAs in Ta-Mo-Cr-Ti-Al system during oxidation at 1200°C. The experimental results lead to the conclusion that the metallic elements have oxidation states Cr^{3+}, Ti^{4+}, Ta^{5+} in the rutile (Cr,Ta,Ti)O_2 oxide formed on equiatomic TaMoCrTiAl and TaMoCr10TiAl. The enhanced Ti concentration in (Cr,Ta,Ti)O_2 reduces the oxygen permeability improving the diffusion properties. Cations Ti^{4+} appear to occupy Cr^{3+} lattice sites leading to reduced oxygen vacancy concentration and consequently thinner oxide scales and zones of internal corrosion. (Cr,Ta,Ti)O_2 reveals perspective protective properties as it possesses higher thermodynamic stability as well as lower growth rates compared to widely accepted chromia scales.

Acknowledgment

The financial support by Deutsche Forschungsgemeinschaft (DFG), grant no. GO 2283/4-2 and HE 1872/34-2 is gratefully acknowledged. Part of this work was performed at the DFG-funded Micro-and Nanoanalytics Facility (MNaF) of the University of Siegen (INST 221/131-1) utilizing its major TEM instrumentation (DFG INST 221/93-1, DFG INST 221/126-1) and sample preparation equipment.

Author contributions

Steven Schellert: Writing - Original Draft, Validation, Investigation, Visualization
Bronislava Gorr: Conceptualization, Visualization, Supervision, Project administration, Formal analysis, Funding acquisition, Writing – Review & Editing
Mathias Galetz: Conceptualization, Formal analysis, Writing – Review & Editing, Visualization, Formal analysis
Christian Wiktor: Investigation, Resources, Visualization, Writing – Review & Editing
Stephan Laube: Visualization, Writing – Review & Editing
Matthias Weber: Visualization, Investigation,
Alexander Kauffmann: Formal analysis, Resources, Visualization, Writing – Review & Editing
Martin Heilmaier: Conceptualization, Resources, Funding acquisition, Writing – Review & Editing
Hans-Jürgen Christ: Conceptualization, Resources, Writing – Review & Editing, Formal analysis
Benjamin Butz: Investigation, Resources, Visualization, Writing – Review & Editing

Data availability

The data that support the finding of this study are available as supplementary materials or from the corresponding author upon reasonable request.

REFERENCES

[1] S. K. Dewangan, A. Mangish, S. Kumar, A. Sharma, B. Ahn, V. Kumar, A review on high-temperature applicability: A milestone for high entropy alloys, Engineering Science and Technology, 35 (2022) 101211. https://doi.org/10.1016/j.jestch.2022.101211.

[2] D. Mitrica, I. C. Badea, B. A. Serban, M. T. Olaru, D. Vonica, M. Burada, R.-R. Piticescu, V. V. Popov, Complex concentrated alloys for substitution of critical raw materials in applications for extreme conditions, Materials 14 (2021) 1197. https://doi.org/10.3390/ma14051197.

[3] O. N. Senkov, G. B. Wilks, J. M. Scott, D. B. Miracle, Mechanical properties of $Nb_{25}Mo_{25}Ta_{25}W_{25}$ and $V_{20}Nb_{20}Mo_{20}Ta_{20}W_{20}$ refractory high entropy alloys, Intermetallics 19 (2011) 698–706. https://doi.org/10.1016/j.intermet.2011.01.004.

[4] O. N. Senkov, D. B. Miracle, K. J. Chaput, J.-P. Couzinie, Development and exploration of refractory high entropy alloys—A review, Journal of Materials Research 33 (2018) 3092–3128. https://doi.org/10.1557/jmr.2018.153.

[5] D. B. Miracle and O. N. Senkov, A critical review of high entropy alloys and related concepts, Acta Materialia 122 (2017) 448–511. https://doi.org/10.1016/j.actamat.2016.08.081.

[6] O. N. Senkov, G. B. Wilks, D. B. Miracle, C. P. Chuang, P. K. Liaw, Refractory high-entropy alloys, Intermetallics 18 (2010) 1758–1765. https://doi.org/10.1016/j.intermet.2010.05.014.

[7] Y. Rao, C. Baruffi, A. de Luca, C. Leinenbach, W. A. Curtin, Theory-guided design of high-strength, high-melting point, ductile, low-density, single-phase BCC high entropy alloys, Acta Materialia 237 (2022) 118132. https://doi.org/10.1016/j.actamat.2022.118132.

[8] N. Yurchenko, E. Panina, Ł. Rogal, L. Shekhawat, S. Zherebtsov, N. Stepanov, Unique precipitations in a novel refractory Nb-Mo-Ti-Co high-entropy superalloy, Materials Research Letters 10 (2022) 78–87. https://doi.org/10.1080/21663831.2021.2022033.

[9] D.-M. Jin, Z.-H. Wang, J.-F. Li, B. Niu, Q. Wang, Formation of coherent BCC/B2 microstructure and mechanical properties of Al–Ti–Zr–Nb–Ta–Cr/Mo light-weight refractory high-entropy alloys, Rare Metals 41 (2022) 2886–2893. https://doi.org/10.1007/s12598-022-01971-w.

[10] F. Liu, P. K. Liaw, Y. Zhang, Recent progress with BCC-structured high-entropy alloys, Metals 12 (2022) 501. https://doi.org/10.3390/met12030501.

[11] T.-X. Li, J.-W. Miao, E.-Y. Guo, H. Huang, J. Wang, Y.-P. Lu, T.-M. Wang, Z.-Q. Cao, T.-J. Li, Tungsten-containing high-entropy alloys: a focused review of manufacturing routes, phase selection, mechanical properties, and irradiation resistance properties, Tungsten 3 (2021) 181–196. https://doi.org/10.1007/s42864-021-00081-x.

[12] M. Srikanth, A. R. Annamalai, A. Muthuchamy, C.-P. Jen, A review of the latest developments in the field of refractory high-entropy alloys, Crystals 11 (2021) 612. https://doi.org/10.3390/cryst11060612.

[13] W. Xiong, A. X. Y. Guo, S. Zhan, C.-T. Liu, J.-W. Yeh, S. C. Cao, Refractory high-entropy alloys: A focused review of preparation methods and properties, Journal of Materials Science & Technology 142 (2022) 196-215. https://doi.org/10.1016/j.jmst.2022.08.046.

[14] K.-C. Lo, H. Murakami, U. Glatzel, J.-W. Yeh, S. Gorsse, A.-C. Yeh, Elemental effects on the oxidation of refractory compositionally complex alloys, International Journal of Refractory Metals and Hard Materials 108 (2022) 105918. https://doi.org/10.1016/j.ijrmhm.2022.105918.

[15] S. Chen, C. Qi, J. Liu, J. Zhang, Y. Wu, Recent advances in W-containing refractory high-entropy alloys—An overview, Entropy 24 (2022) 1553. https://doi.org/10.3390/e24111553.

[16] S. Lu, X. Li, X. Liang, W. Yang, J. Chen, Effect of V and Ti on the oxidation resistance of WMoTaNb refractory high-entropy alloy at high temperatures, Metals 12 (2022) 41. https://doi.org/10.3390/met12010041.

[17] T. M. Butler, K. J. Chaput, J. R. Dietrich, O. N. Senkov, High temperature oxidation behaviors of equimolar NbTiZrV and NbTiZrCr refractory complex concentrated alloys (RCCAs), Journal of Alloys and Compounds 729 (2017) 1004–1019. https://doi.org/10.1016/j.jallcom.2017.09.164.

[18] O. N. Senkov, S. V. Senkova, D. M. Dimiduk, C. Woodward, D. B. Miracle, Oxidation behavior of a refractory $NbCrMo_{0.5}Ta_{0.5}TiZr$ alloy, Journal of Materials Science 47 (2012) 6522–6534. https://doi.org/10.1007/s10853-012-6582-0.
[19] Y. Xiao, W. Kuang, Y. Xu, L. Wu, W. Gong, J. Qian, Q. Zhang, Y. He, Microstructure and oxidation behavior of the CrMoNbTaV high-entropy alloy, Journal of Materials Research 34 (2019) 301–308. https://doi.org/10.1557/jmr.2018.340.
[20] N. Birks, G. H. Meier, F. S. Pettit, Introduction to the high temperature oxidation of metals, second edition, Cambridge University Press, Cambridge, 2006.
[21] T. Fu, K. Cui, Y. Zhang, J. Wang, X. Zhang, F. Shen, L. Yu, H. Mao, Microstructure and oxidation behavior of anti-oxidation coatings on Mo-based alloys through HAPC process: A review, Coatings 11 (2021) 883. https://doi.org/10.3390/coatings11080883.
[22] X. Ren, Y. Li, Y. Qi, B. Wang, Review on preparation technology and properties of refractory high entropy alloys, Materials 15 (2022) 2931. https://doi.org/10.3390/ma15082931.
[23] R. Bürgel, Handbuch Hochtemperatur-Werkstofftechnik: Grundlagen, Werkstoffbeanspruchungen, Hochtemperaturlegierungen und -beschichtungen ; mit 70 Tabellen, third edition, Vieweg, Wiesbaden, 2006.
[24] S. D. Cramer, ASM Handbook Volume 13B, Corrosion: Materials, ASM International, Materials Park, Ohio, 2005.
[25] T. E. Tietz and J. W. Wilson, Behavior and properties of refractory metals, Stanford University Press, Stanford, 1965.
[26] L. La, L. Wang, F. Liang, J. Zhang, L. Qin, B. Tang, Y. Wu, Tribological behaviors and high-temperature oxidation resistance properties of WTaVCr alloy coating, Social Science Research Network (2022). https://doi.org/10.2139/ssrn.4181386.
[27] H. Okamoto, O-Zr (Oxygen-Zirconium), Journal of Phase Equilibria and Diffusion 28 (2007) 498. https://doi.org/10.1007/s11669-007-9154-2.
[28] R. F. Domagala and R. Ruh, ASM Transactions Quarterly (1965) 164.
[29] E. H. Copland, N. S. Jacobson, K. Hilpert, D. Kath, Thermodynamics of the Ti–Al–O system, Calphad 77 (2022) 102400. https://doi.org/10.1016/j.calphad.2022.102400.
[30] H. Okamoto, O-Ti (Oxygen-Titanium), Journal of Phase Equilibria and Diffusion 32 (2011) 473–474. https://doi.org/10.1007/s11669-011-9935-5.
[31] J. Veverka, M. Vilémová, Z. Chlup, H. Hadraba, F. Lukáč, Š. Csáki, J. Matějíček, J. Vontorová, T. Chráska, Evolution of carbon and oxygen concentration in tungsten prepared by field assisted sintering and its effect on ductility, International Journal of Refractory Metals and Hard Materials 97 (2021) 105499. https://doi.org/10.1016/j.ijrmhm.2021.105499.
[32] W. D. Klopp, Recent developments in chromium and chromium alloys, NASA-report TM X-1867 (1969).
[33] L. Yu, Y. Zhang, T. Fu, J. Wang, K. Cui, F. Shen, Rare earth elements enhanced the oxidation resistance of Mo-Si-based alloys for high temperature application: A review, Coatings 11 (2021) 1144. https://doi.org/10.3390/coatings11091144.
[34] R. Anton, S. Hüning, N. Laska, M. Weber, S. Schellert, B. Gorr, H.-J. Christ, U. Schulz, Graded PVD Mo-Si interlayer between Si coating and Mo-Si-B alloys: Investigation of oxidation behaviour, Corrosion Science 192 (2021) 109843. https://doi.org/10.1016/j.corsci.2021.109843.
[35] S. Ma, Q. Ding, X. Wei, Z. Zhang, H. Bei, The effects of alloying elements Cr, Al, and Si on oxidation behaviors of Ni-based superalloys, Materials 15 (2022) 7352. https://doi.org/10.3390/ma15207352.
[36] W. Gui, Y. Liang, J. Qin, Y. Wang, J. Lin, Fluorine effect for improving oxidation resistance of Ti-45Al-8.5Nb alloy at 1000 °C, Materials 15 (2022) 2767. https://doi.org/10.3390/ma15082767.
[37] M. Wu, B. Zheng, D. Zhang, T. Huang, C. Li, Q. Li, W. Huang, L. Zhang, P. Song, Effect of water vapor on the microstructure of Al_2O_3 on the free-standing MCrAlY alloy at 1100 °C, Metals 12 (2022) 865. https://doi.org/10.3390/met12050865.
[38] M. H. Ani, H. Purwanto, M. Musa, S. Illias, A. Kaderi, N. Salim, M. H. A. Rahim, A. G. E. Sutjipto, Electrochemical monitoring of oxygen potential on Fe-Cr alloy surface during high temperature oxidation in dry and humid Conditions, Proceedings of the 7th International Corrosion Prevention Symposium for Research Scholars, Springer Nature Singapore, Singapore, 2023, pp. 217–228.
[39] X. H. Wang and Y. C. Zhou, High-temperature oxidation behavior of Ti_2AlC in air. Oxidation of Metals 59 (2003) 303-320. https://doi.org/10.1023/A:1023092027697.
[40] Y. Hua, Z. Rong, Y. Ye, K. Chen, R. Chen, Q. Xue, H. Liu, Laser shock processing effects on isothermal oxidation resistance of GH586 superalloy, Applied Surface Science 330 (2015) 439–444. https://doi.org/10.1016/j.apsusc.2015.01.033.

[41] M. A. Azim, D. Schliephake, C. Hochmuth, B. Gorr, H.-J. Christ, U. Glatzel, M. Heilmaier, Creep resistance and oxidation behavior of novel Mo-Si-B-Ti alloys, JOM 67 (2015) 2621–2628. https://doi.org/10.1007/s11837-015-1560-z.

[42] O. A. Waseem, U. Auyeskhan, H. M. Lee, H. J. Ryu, A combinatorial approach for the synthesis and analysis of $Al_xCr_yMo_zNbTiZr$ high-entropy alloys: Oxidation behavior, Journal of Materials Research 33 (2018) 3226–3234. https://doi.org/10.1557/jmr.2018.241.

[43] J. Jayaraj, P. Thirathipviwat, J. Han, A. Gebert, Microstructure, mechanical and thermal oxidation behavior of AlNbTiZr high entropy alloy, Intermetallics 100 (2018) 9–19. https://doi.org/10.1016/j.intermet.2018.05.015.

[44] S. Sheikh, M. K. Bijaksana, A. Motallebzadeh, S. Shafeie, A. Lozinko, L. Gan, T.-K. Tsao, U. Klement, D. Canadinc, H. Murakami, S. Guo, Accelerated oxidation in ductile refractory high-entropy alloys, Intermetallics 97 (2018) 58–66. https://doi.org/10.1016/j.intermet.2018.04.001.

[45] F. Müller, B. Gorr, H.-J. Christ, J. Müller, B. Butz, H. Chen, A. Kauffmann, M. Heilmaier, On the oxidation mechanism of refractory high entropy alloys, Corrosion Science 159 (2019) 108161. https://doi.org/10.1016/j.corsci.2019.108161.

[46] S. Schellert, B. Gorr, H.-J. Christ, C. Pritzel, S. Laube, A. Kauffmann, M. Heilmaier, The effect of Al on the formation of a $CrTaO_4$ layer in refractory high entropy alloys Ta-Mo-Cr-Ti-xAl, Oxidation of Metals 96 (2021) 333–345. https://doi.org/10.1007/s11085-021-10046-7.

[47] S. Schellert, B. Gorr, S. Laube, A. Kauffmann, M. Heilmaier, H.-J. Christ, Oxidation mechanism of refractory high entropy alloys Ta-Mo-Cr-Ti-Al with varying Ta content, Corrosion Science 192 (2021) 109861. https://doi.org/10.1016/j.corsci.2021.109861.

[48] C.-H. Chang, M. S. Titus, J.-W. Yeh, Oxidation behavior between 700 and 1300 °C of refractory TiZrNbHfTa high-entropy alloys containing aluminum, Advanced Engineering Materials 20 (2018) 1700948. https://doi.org/10.1002/adem.201700948.

[49] S. K. Varma, F. Sanchez, S. Moncayo, C. V. Ramana, Static and cyclic oxidation of Nb-Cr-V-W-Ta high entropy alloy in air from 600 to 1400 °C, Journal of Materials Science & Technology 38 (2020) 189–196. https://doi.org/10.1016/j.jmst.2019.09.005.

[50] J. Spyridelis, P. Delavignette, S. Amelinckx, On the Superstructures of Ta_2O_5 and Nb_2O_5, Physica Status Solidi (b) 19 (1967) 683–704. https://doi.org/10.1002/pssb.19670190220.

[51] H. Schäfer, R. Gruehn, F. Schulte, The Modifications of Niobium Pentoxide, Angewandte Chemie International Edition in English 5 (1966) 40–52. https://doi.org/10.1002/anie.196600401.

[52] N. Esparza, V. Rangel, A. Gutierrez, B. Arellano, S. K. Varma, A comparison of the effect of Cr and Al additions on the oxidation behaviour of alloys from the Nb–Cr–Si system, Materials at High Temperatures 33 (2016) 105–114. https://doi.org/10.1179/1878641315Y.0000000012.

[53] M. P. Arbuzov and V. G. Chuprina, The oxidation of niobium and the structure of niobium oxides, Soviet Physics Journal 8 (1966) 87–89. https://doi.org/10.1007/BF00838593.

[54] C. M. Liu, H. M. Wang, S. Q. Zhang, H. B. Tang, A. L. Zhang, Microstructure and oxidation behavior of new refractory high entropy alloys, Journal of Alloys and Compounds 583 (2014) 162–169. https://doi.org/10.1016/j.jallcom.2013.08.102.

[55] K.-C. Lo, Y.-J. Chang, H. Murakami, J.-W. Yeh, A.-C. Yeh, An oxidation resistant refractory high entropy alloy protected by $CrTaO_4$-based oxide, Scientific reports 9 (2019) 7266. https://doi.org/10.1038/s41598-019-43819-x.

[56] M. Ghadyani, C. Utton, P. Tsakiropoulos, Microstructures and isothermal oxidation of the alumina scale forming $Nb_{1.7}Si_{2.4}Ti_{2.4}Al_3Hf_{0.5}$ and $Nb_{1.3}Si_{2.4}Ti_{2.4}Al_{3.5}Hf_{0.4}$alloys, Materials 12 (2019) 222. https://doi.org/10.3390/ma12020222.

[57] K.-C. Lo, H. Murakami, J.-W. Yeh, A.-C. Yeh, Oxidation behaviour of a novel refractory high entropy alloy at elevated temperatures, Intermetallics 119 (2020) 106711. https://doi.org/10.1016/j.intermet.2020.106711.

[58] B. Gorr, F. Müller, S. Schellert, H.-J. Christ, H. Chen, A. Kauffmann, M. Heilmaier, A new strategy to intrinsically protect refractory metal based alloys at ultra high temperatures, Corrosion Science 166 (2020) 108475. https://doi.org/10.1016/j.corsci.2020.108475.

[59] C.-N. Huang, J.-S. Bow, Y. Zheng, S.-Y. Chen, N. Ho, P. Shen, Nonstoichiometric titanium oxides via pulsed laser ablation in water, Nanoscale Research Letters 5 (2010) 972–985. https://doi.org/10.1007/s11671-010-9591-4.

[60] M. P. Brady, P. F. Tortorelli, E. A. Payzant, L. R. Walker, Oxidation behavior of Cr_2N, CrNbN, and CrTaN phase mixtures formed on nitrided Cr and Laves-reinforced Cr alloys, Oxidation of Metals 61 (2004) 379–401. https://doi.org/10.1023/B:OXID.0000032330.95411.EC.

[61] S. Turner, S. Lazar, B. Freitag, R. Egoavil, J. Verbeeck, S. Put, Y. Strauven, G. van Tendeloo, High resolution mapping of surface reduction in ceria nanoparticles, Nanoscale 3 (2011) 3385–3390. https://doi.org/10.1039/C1NR10510H.

[62] H. Tan, S. Turner, E. Yücelen, J. Verbeeck, G. van Tendeloo, 2D atomic mapping of oxidation states in transition metal oxides by scanning transmission electron microscopy and electron energy-loss spectroscopy, Physical Review Letters 107 (2011) 107602. https://doi.org/10.1103/PhysRevLett.107.107602.

[63] K. Suenaga and M. Koshino, Atom-by-atom spectroscopy at graphene edge, Nature 468 (2010) 1088–1090. https://doi.org/10.1038/nature09664.

[64] M. A. Azim, H.-J. Christ, B. Gorr, T. Kowald, O. Lenchuk, K. Albe, M. Heilmaier, Effect of Ti addition on the thermal expansion anisotropy of Mo_5Si_3, Acta Materialia 132 (2017) 25–34. https://doi.org/10.1016/j.actamat.2017.02.066.

[65] H. Chen, A. Kauffmann, S. Seils, T. Boll, C. H. Liebscher, I. Harding, K. S. Kumar, D. V. Szabó, S. Schlabach, S. Kauffmann-Weiss, F. Müller, B. Gorr, H.-J. Christ, M. Heilmaier, Crystallographic ordering in a series of Al-containing refractory high entropy alloys Ta–Nb–Mo–Cr–Ti–Al, Acta Materialia 176 (2019) 123–133. https://doi.org/10.1016/j.actamat.2019.07.001.

[66] W. Ren, F. Ouyang, B. Ding, Y. Zhong, J. Yu, Z. Ren, L. Zhou, The influence of $CrTaO_4$ layer on the oxidation behavior of a directionally-solidified nickel-based superalloy at 850–900 °C, Journal of Alloys and Compounds 724 (2017) 565–574. https://doi.org/10.1016/j.jallcom.2017.07.066.

[67] P. Massard, J. C. Bernier, A. Michel, Effet Jahn-Teller dans le système Ta_2CrO_6-$TaCrO_4$, Journal of Solid State Chemistry 4 (1972) 269–274. https://doi.org/10.1016/0022-4596(72)90116-8.

[68] F. Schlottig, J. Schreckenbach, G. Marx, Preparation and characterisation of chromium and sodium tantalate layers by anodic spark deposition, Fresenius' Journal of Analytical Chemistry 363 (1999) 209–211. https://doi.org/10.1007/s002160051174.

[69] R. Mani, S. N. Achary, K. R. Chakraborty, S. K. Deshpande, J. E. Joy, A. Nag, J. Gopalakrishnan, A.K. Tyagi, $FeTiTaO_6$: A lead-free relaxor ferroelectric based on the rutile structure, Advanced Materials 20 (2008) 1348–1352. https://doi.org/10.1002/adma.200701940.

[70] S. P. McBride and R. Brydson, Analytical transmission electron microscopy and surface spectroscopy of ceramics: The microstructural evolution in titanium-doped chromia polycrystals as a function of sintering conditions, Journal of Materials Science 39 (2004) 6723–6734. https://doi.org/10.1023/B:JMSC.0000045602.50785.f3.

[71] P. Ewels, T. Sikora, V. Serin, C. P. Ewels, L. Lajaunie, A complete overhaul of the electron energy-loss spectroscopy and X-ray absorption spectroscopy database: eelsdb.eu, Microscopy and Microanalysis 22 (2016) 717–724. https://doi.org/10.1017/S1431927616000179.

[72] J. H. Perepezko, F. Rioult, R. Sakidja, Oxidation performance of high temperature Mo-Si-B alloys and coatings, Materials Science Forum Volumes 595-598 (2008) 1065–1074. https://doi.org/10.4028/www.scientific.net/MSF.595-598.1065.

[73] E. A. Gulbransen, K. F. Andrew, F. A. Brassart, Oxidation of molybdenum 550° to 1700°C, Journal of The Electrochemical Society 110 (1963) 952–959.

[74] L. Qin, Y. Pei, S. Li, X. Zhao, S. Gong, H. Xu, Role of volatilization of molybdenum oxides during the cyclic oxidation of high-Mo containing Ni-based single crystal superalloys, Corrosion Science 129 (2017) 192–204. https://doi.org/10.1016/j.corsci.2017.08.025.

[75] J. Li, Y. Chen, Y. Li, Z. Bai, K. Wang, Influence of aluminium addition on oxidation resistance of Ta-W alloy, Powder Metallurgy 62 (2019) 322–330. https://doi.org/10.1080/00325899.2019.1662559.

[76] H. Mitsui, H. Habazaki, K. Hashimoto, S. Mrowec, The sulfidation and oxidation behavior of sputter-deposited Al-Ta alloys at high temperatures, Corrosion Science 39 (1997) 59–76. https://doi.org/10.1016/S0010-938X(96)00104-7.

[77] A. Jalowicka, W. Nowak, D. Naumenko, L. Singheiser, W. J. Quadakkers, Effect of nickel base superalloy composition on oxidation resistance in SO_2 containing, high pO_2 environments, Materials and Corrosion 65 (2014) 178–187. https://doi.org/10.1002/maco.201307299.

[78] W. J. Nowak, B. Wierzba, J. Sieniawski, Effect of Ti and Ta on oxidation kinetic of chromia forming Ni-base superalloys in Ar-O_2-based atmosphere, High Temperature Materials and Processes 37 (2018) 801–806. https://doi.org/10.1515/htmp-2017-0089.

[79] S.-J. Park, S.-M. Seo, Y.-S. Yoo, H.-W. Jeong, H. Jang, Effects of Al and Ta on the high temperature oxidation of Ni-based superalloys, Corrosion Science 90 (2015) 305–312. https://doi.org/10.1016/j.corsci.2014.10.025.

[80] H.-S. Kim, S.-J. Park, S.-M. Seo, Y.-S. Yoo, H.-W. Jeong, H. Jang, High temperature oxidation resistance of Ni-(5~13)Co-(10~16)Cr-(5~9)W-5Al-(1~1.5)Ti-(3~6)Ta alloys, Metals and Materials International 22 (2016) 789–796. https://doi.org/10.1007/s12540-016-6305-1

[81] R. Mani, S. N. Achary, K. R. Chakraborty, S. K. Deshpande, J. E. Joy, A. Nag, J. Gopalakrishnan, A. K. Tyagi, Dielectric properties of some $MM'O_4$ and $MTiM'O_6$ (M=Cr, Fe, Ga; M′=Nb, Ta, Sb) rutile-type oxides, Journal of Solid State Chemistry 183 (2010) 1380–1387. https://doi.org/10.1016/j.jssc.2010.04.022.

[82] A. Petersen and H. Müller-Buschbaum, Ein Beitrag über Oxide vom Typ AMO_4 (A = Ti^{3+}, Cr^{3+}; M = Nb^{5+}, Ta^{5+}), Zeitschrift für anorganische und allgemeine Chemie 609 (1992) 51–54. https://doi.org/10.1002/zaac.19926090309.

[83] G. Sarazin, Comptes Rendus Hebdomadaires des Seances de l'Academie des Sciences 815–817.

[84] B. Jasper-Tönnies and H. Müller-Buschbaum, Synthese und Struktur von $AlTaO_4$, Zeitschrift für anorganische und allgemeine Chemie 504 (1983) 113–116. https://doi.org/10.1002/zaac.19835040914.

[85] D. N. Astrov, N. A. Kryukova,R. B. Zorin, V. A. Makarov, R. P. Ozerov, F. A. Rozhdestvenskii, V. P. Smirnov, A. M. Turchaninov, N. V. Fadeeva, Atomic and molecular ordering in MeTaO4 (Me=Ti,V, Cr,Fe) with a rutile structure, Kristallografiya 17 (1972) 1152–1161.

[86] E. Peters, H. Müller Buschbaum, Ein Titan-Tantaloxid mit Ti^{II}: $Ti_{0,33}Ta_{0,67}O_2$ ($TiTa_2O_6$), Zeitschrift für Naturforschung, B: Anorganische Chemie 50 (1995) 1167–1170.

[87] K. Sugiyama, Y. Takeuchi, The crystal structure of rutile as a function of temperature up to 1600°C, Zeitschrift für Kristallographie - Crystalline Materials 194 (1991) 305–313. https://doi.org/10.1524/zkri.1991.194.3-4.305.

[88] W. H. Baur and A. A. Khan, Rutile-type compounds. IV. SiO_2, GeO_2 and a comparison with other rutile-type structures, Acta Crystallographica Section B 27 (1971) 2133–2139. https://doi.org/10.1107/S0567740871005466.

[89] S. E. Rasmussen, Relative merits of reflection and transmission techniques in laboratory powder diffraction, Powder Diffraction 18 (2003) 281–284. https://doi.org/10.1154/1.1633563.

[90] J. Li, G. Song, M. Wang, B. Zhang, Study on phase relations, crystal sttructure and magnetic properties of $Ti_{1-x}Cr_xO_{2+d}$ system, Wuli Xuebao 56 (2007) 3379–3387.

[91] W. Wong-Ng, H. F. McMurdie, C. R. Hubbard, A. D. Mighell, JCPDS-ICDD Research Associateship (Cooperative Program with NBS/NIST): PDF No. 39-1428, Journal of Research of the National Institute of Standards and Technology 106 (2001) 1013–1028. https://doi.org/10.6028/jres.106.052.

Supplementary Material

Material S1

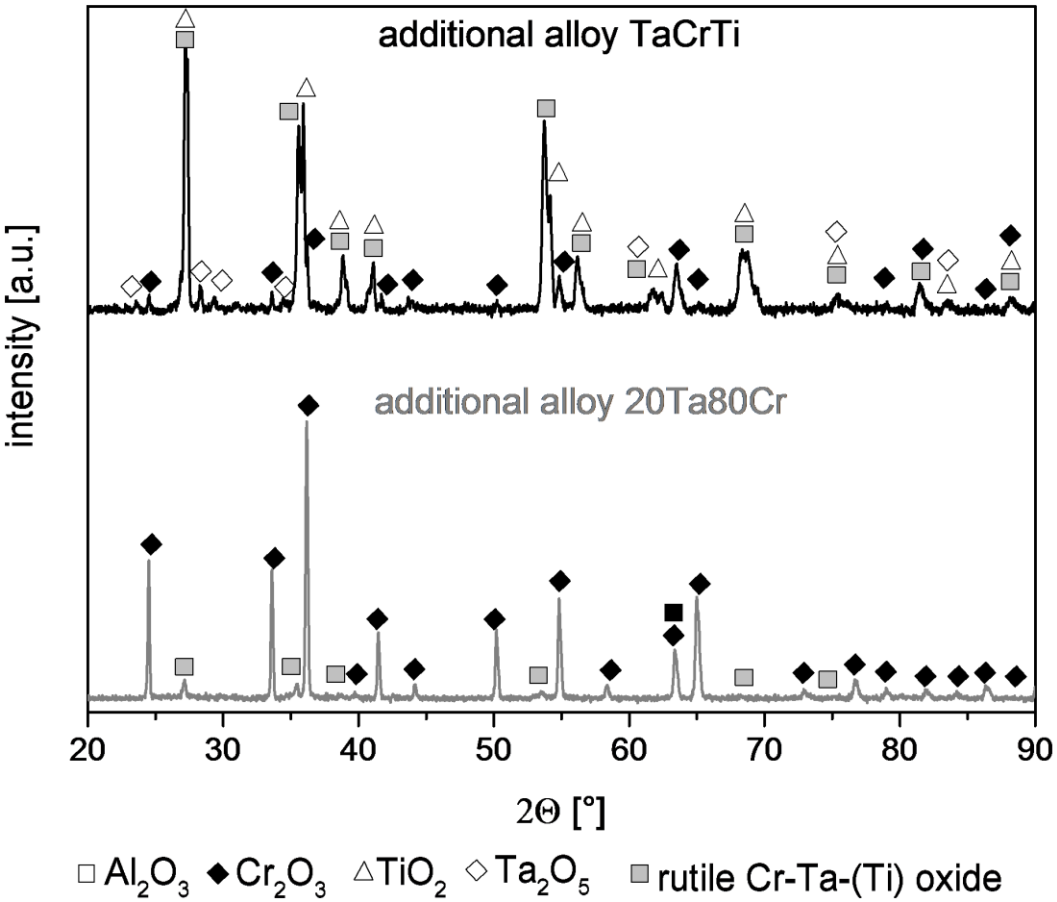

Fig S. 1 XRD pattern of additional alloys 20Ta80Cr and TaCrTi after oxidation to air at 1200 °C for 24 h. The peaks are labeled according to simulated XRD data based on the structures of the oxides listed in the legend.

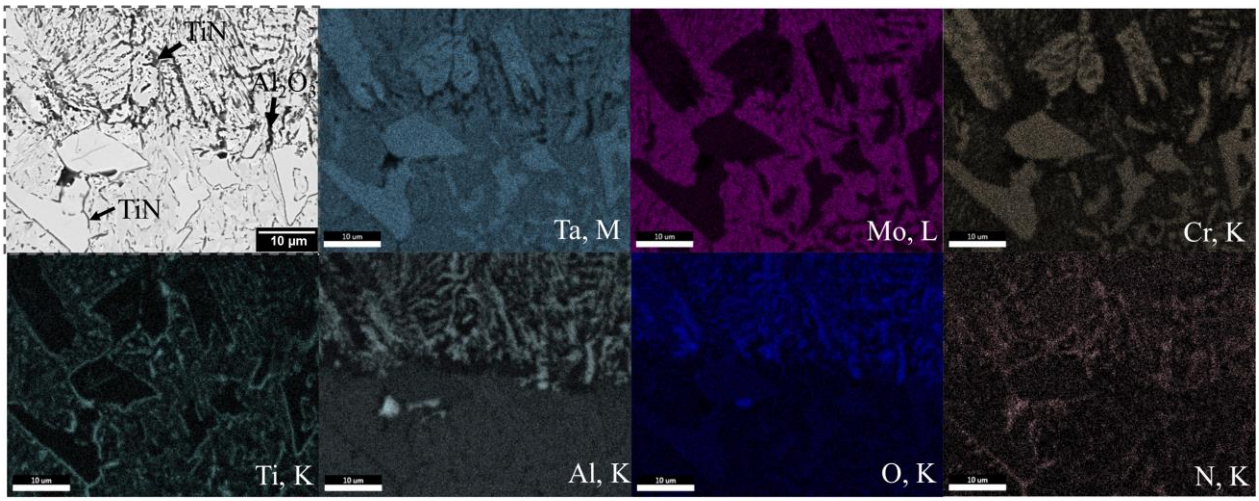

Fig S. 2 BSE-SEM image of details of the internal corrosion zone in TaMoCr10TiAl (marked area in Fig. 6 b. after exposure to air at 1200 °C for 24 h and the corresponding EDX-mapping.

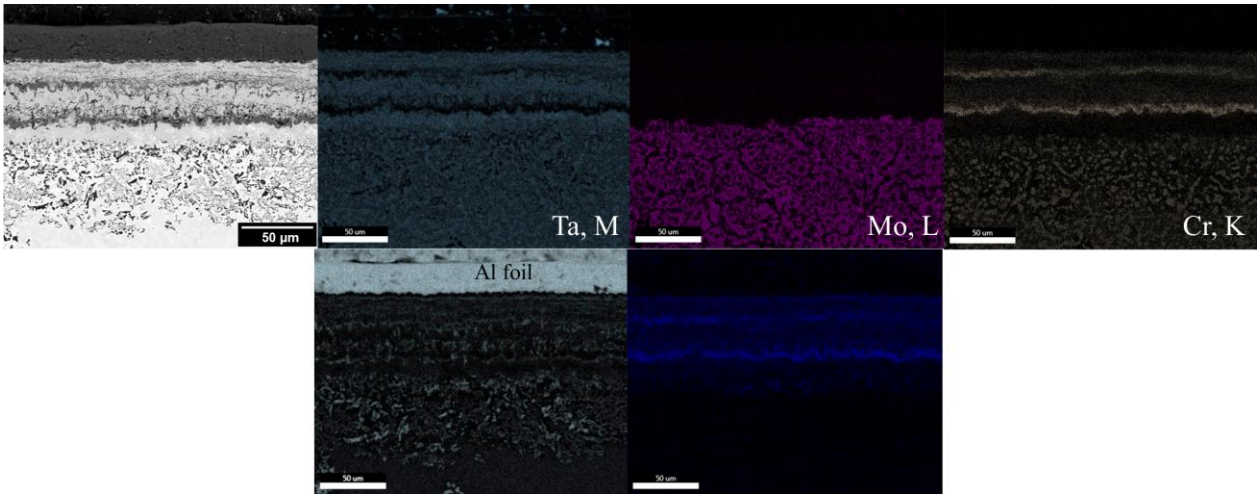

Fig S. 3 BSE-SEM micrograph of oxide scale formed on TaMoCrAl after exposure to air at 1200 °C for 24 h and the corresponding EDX-mapping.

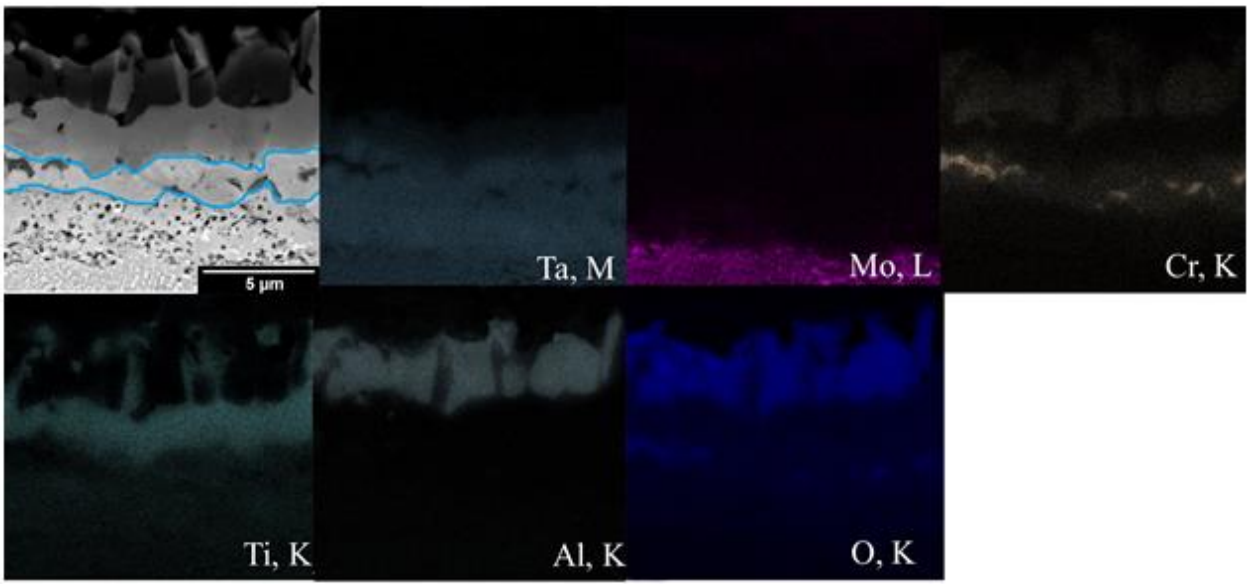

Fig S. 4 BSE-SEM micrograph of outer oxide scale formed on TaMoCr10TiAl after exposure to air at 1200 °C for 24 h and the corresponding EDX-mapping. The $(Cr,Ta,Ti)O_2$ scale is highlighted in the BSE-SEM image.

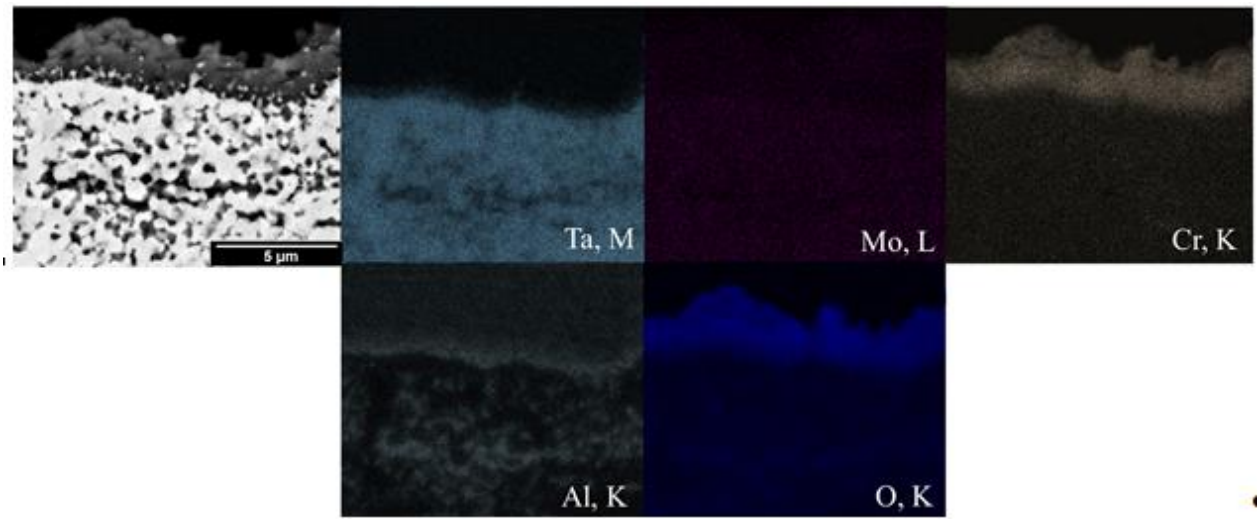

Fig S. 5 BSE-SEM micrograph of the outer oxide scale formed on TaMoCrAl after exposure to air at 1200 °C for 24 h and the corresponding EDX-mapping.

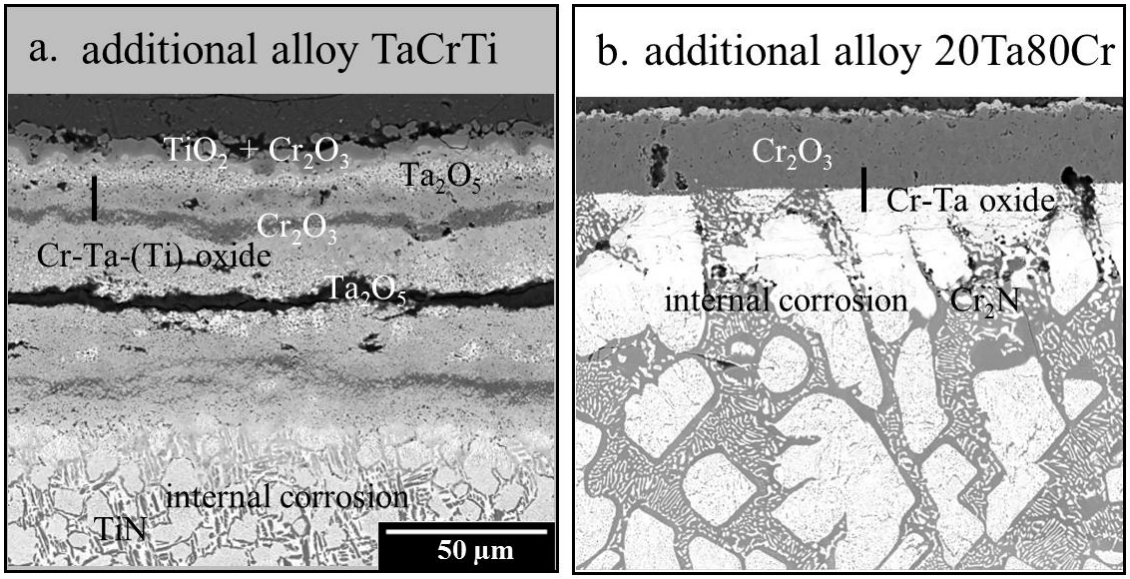

Fig S. 6 BSE-SEM images of formed oxide scale on additional alloys (a.) TaCrTi and (b.) 20Ta80Cr after exposure to air at 1200 °C for 24h. The vertical black line mark indicates the position of TEM lamella.

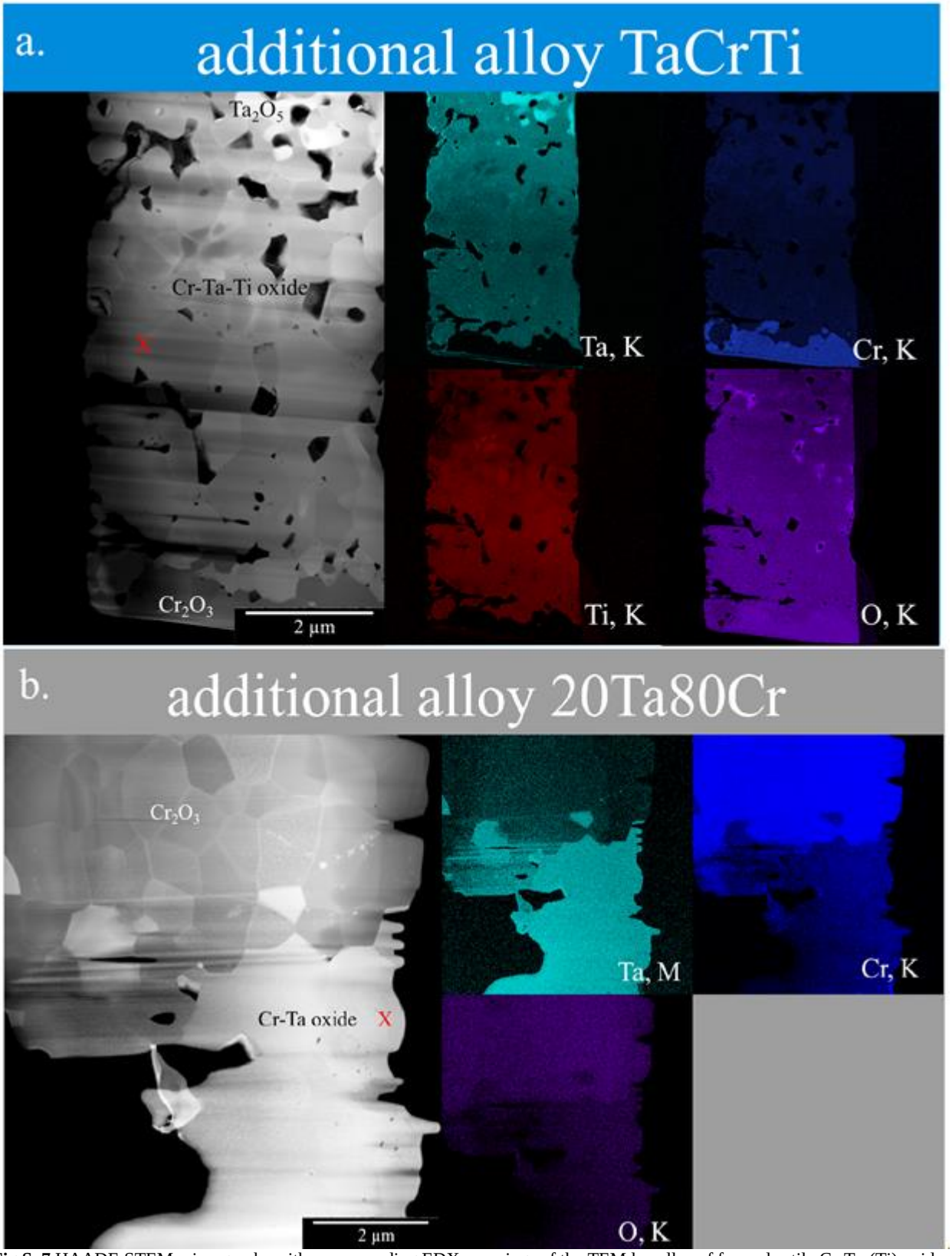

Fig S. 7 HAADF-STEM micrographs with corresponding EDX mappings of the TEM lamellae of formed rutile Cr-Ta-(Ti) oxides on additional alloys TaCrTi (a.) and (b.) 20Ta80Cr after oxidation to air at 1200 °C for 24 h. The "X" marks the location of the EELS records.

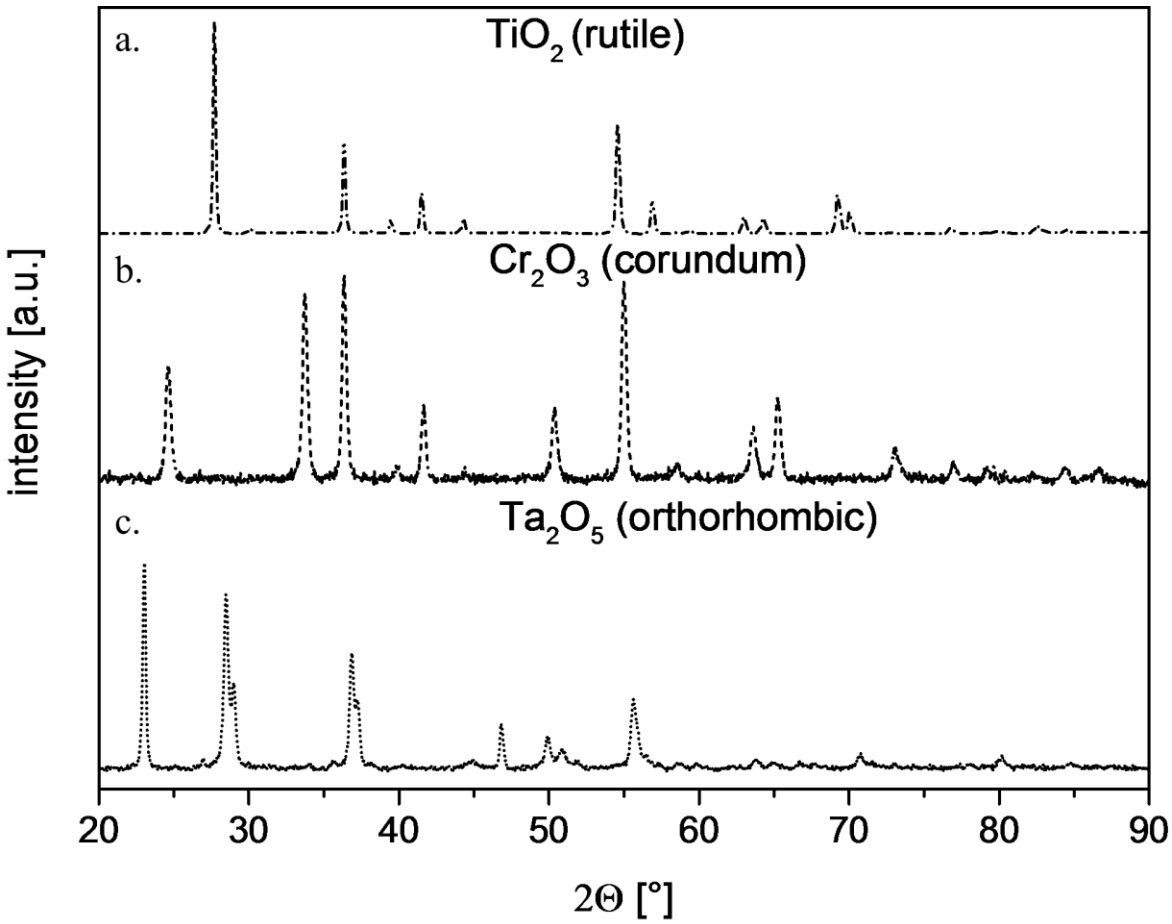

Fig S. 8 XRD analysis of reference powder (a.) TiO_2, (b.) Cr_2O_3 and (c.) Ta_2O_5

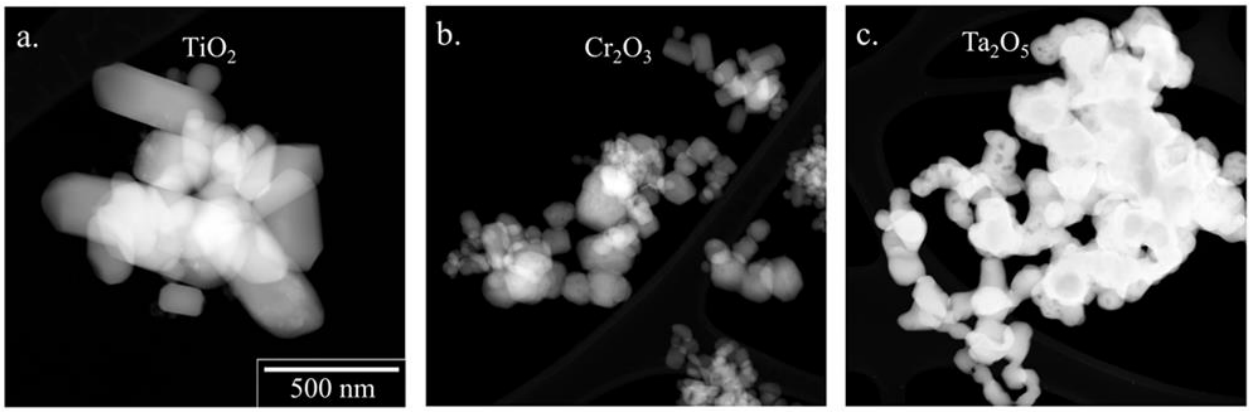

Fig S. 9 HAADF-STEM micrographs of reference powder: a. TiO_2, b. Cr_2O_3 and c. Ta_2O_5.